GSI

Report 2001 - 06
December

Schottky mass measurements of cooled nuclei and mass landscape of the new area of neutron-deficient sub-uranium nuclides

T. Radon, Yu.N. Novikov, H. Geissel, G. Münzenberg, F. Attallah, K. Beckert, T. Beha, F. Bosch, H. Eickhoff, M. Falch, B. Franzke, Y. Fujita, M. Hausmann, F. Herfurth, H. Irnich, H.C. Jung, Th. Kerscher, O. Klepper, H.-J. Kluge, C. Kozhuharov, Yu.A. Litvinov, K.E.G. Löbner, F. Nickel, F. Nolden, Z. Patyk, H. Reich, C. Scheidenberger, W. Schwab, B. Schlitt, M. Steck, K. Sümmerer, A.H. Wapstra, Th. Winkler, H. Wollnik

Gesellschaft für Schwerionenforschung mbH
Planckstraße 1 • D-64291 Darmstadt • Germany
Postfach 11 05 52 • D-64220 Darmstadt • Germany

Schottky mass measurements of cooled nuclei and mass landscape of the new area of neutron-deficient sub-uranium nuclides

December 12, 2001

T. Radon[1], Yu. N. Novikov[1,2,3], H. Geissel[1,4], G. Münzenberg[1,5], F. Attallah[1], K. Beckert[1], T. Beha[6], F. Bosch[1], H. Eickhoff[1], M. Falch[6], B. Franzke[1], Y. Fujita[7], M. Hausmann[1], F. Herfurth[1], H. Irnich[1], H. C. Jung[4], Th. Kerscher[6], O. Klepper[1], H.-J. Kluge[1], C. Kozhuharov[1], Yu. A. Litvinov[1,3], K. E. G. Löbner[6], F. Nickel[1], F. Nolden[1], Z. Patyk[8], H. Reich[1], C. Scheidenberger[1,4], W. Schwab[1], B. Schlitt[1], M. Steck[1], K. Sümmerer[1], A.H. Wapstra[9], Th. Winkler[1], H. Wollnik[4]

[1] *Gesellschaft für Schwerionenforschung, Planckstrasse 1, D-64291 Darmstadt, Germany*
[2] *St. Petersburg Nuclear Physics Institute, Gatchina 188350, Russia*
[3] *St. Petersburg St. University, St.Petersburg, 198904, Russia*
[4] *II. Physikalisches Institut, Universität Gießen, Heinrich-Buff-Ring 16, D-35392 Gießen, Germany*
[5] *Johannes Gutenberg-Universität Mainz, Mainz, Germany*
[6] *Sektion Physik, Ludwig-Maximilians-Universität München, Am Coulombwall, D-85748 Garching, Germany*
[7] *College of General Education, Osaka University, Osaka 560, Japan*
[8] *Soltan Institute for Nuclear Studies, Warsaw, Poland*
[9] *National Institute of Nuclear Physics and High Energy Physics, NIKHEF, PO Box 41882, 1009DB Amsterdam, The Netherlands*

GSI, Darmstadt,
2001

Abstract

A novel method for direct, high precision mass measurements of relativistic exotic nuclei has been successfully applied in the storage ring ESR at GSI. The nuclei of interest were produced by projectile fragmentation of relativistic highly charged gold and bismuth ions. Products of reactions were separated in-flight by the fragment separator FRS, stored and electron cooled in the storage ring ESR. The mass values have been deduced from the revolution frequencies of the cooled circulating ions, which have been measured by Schottky diagnosis via a Fourier transform of the Schottky noise signal.
The main bulk of information have been obtained by fragmentation of 930 MeV/u bismuth ions and is described in this report. The masses for 104 neutron-deficient nuclides of the elements $57 \leq Z \leq 84$ have been measured for the first time. The precision of mass data obtained is ≈ 100 keV. Using experimentally known energies of α-transitions linking the measured nuclides with long α-decay chains we obtained the masses of further short-lived exotic nuclides in addition and, thus, extended the mass determination to the large area of the nuclear chart up to exotic neutron-deficient sub-uranium nuclides. In total the mass values for 168 nuclides have been determined for the first time. The masses for 60 isomeric states with unknown so far excitation energies have been evaluated as well.
This new large scale information obtained about masses allows a new look to the particular features of physics in the exotic territory of the chart of nuclides. One- and two-proton drip-lines have been identified. No evidence for a Thomas-Ehrman shift which could perturb the position of drip-lines has been observed in the region of heavy nuclides. The size of the "littoral shallow" of the sea of instability were outlined for the heavy mass region. The analysis of information on the new masses shows a washing out of the two-proton separation energy gap for lead nuclides far off the β-stability. The predictive power of various mass models has been tested. The result is that neither of mass formula tested yields mass values for exotic neutron-deficient nuclides with an accuracy better than 400 keV.
The potential of Schottky mass spectrometry in the future has been discussed.

1 Introduction

The mass of a nucleus is a basic property which reflects the combined effects of all forces that act in the nucleus. It determines the stability of the nucleus and gives information about its structure. Systematic studies of nuclear masses as a function of the neutron number N and proton number Z [1] have revealed important properties such as shell closures and changes of the nuclear shape . The mass mapping throughout the nuclear chart allows to investigate global properties of nuclides and of nuclear matter [2]. One can note here the problem of restoration of the Wigner SU_4-symmetry in heavy nuclides [3, 4], the problem of so called curvature [5] and congruent [6] terms, the parametrization of the mass formula by $Z^{2/3}$-term in the nuclear surface [7] etc..
Present nuclear models based on effective nuclear forces and developed from the properties of nuclei close to the valley of β-stability cannot properly handle the isospin and density dependence [8, 9, 10]. Therefore, masses far off stability are sensitive probes for nuclear models [11] and necessary for their further development. Of special interest are the most exotic species located near the drip lines, at closed shells far off stability or along the paths of cosmic nucleosynthesis.

The situation of known and unknown masses before our experiments is shown in Fig. 1.

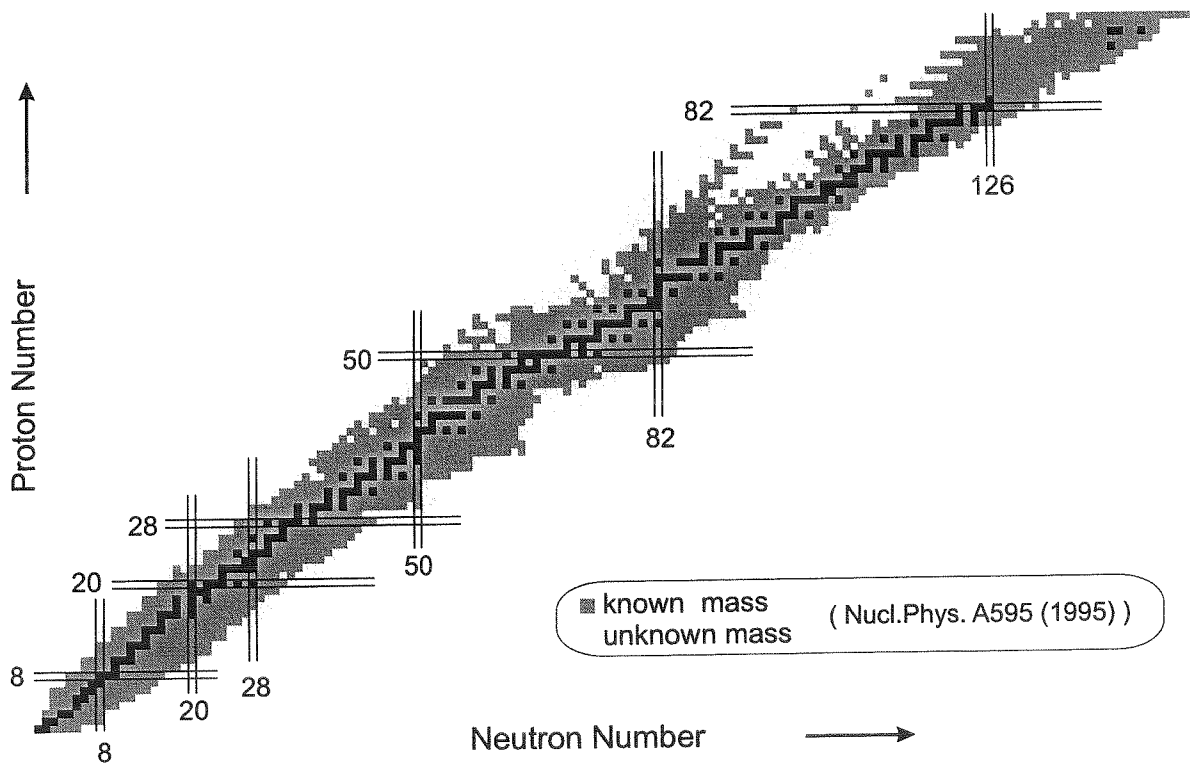

Figure 1: Chart of nuclides with known and unknown masses illustrated according to [13]. The peninsula of unknown massses in the sublead region can be seen

Our knowledge of the experimental mass surface is based on various direct and indirect methods combined with a careful evaluation and adjustment of the set of the experimental data [12, 13]. Fig. 1 shows 1840 nuclides with measured masses and about 1100 known nuclides far from stability which have been observed and whose masses are not

known yet. A review [14] summarizes the experimental and theoretical progress in the field.
The pioneering experiments for mass determination of exotic nuclides used electromagnetic spectrometers [15]. The precision of the conventional spectrometers is limited by the ion-optical resolving power combined with the intensity requirement for exotic nuclei. During the last years a new generation of tecnique for mass measurements has successfully been developed [14, 16, 17, 18]. Dealing with the measurements of time-of-flight or frequency these new methods substituted the conventional methods of the decay Q-value and voltage measurements. The accuracy of Q-value procedure is inherently dependent on a detailed knowledge of the nuclear decay properties. Though the precision of time-of-flight methods is still not high [19, 20], the frequency measurements in two-cyclotron mode [21]-[23] provides more precise mass-values. The highest precision in mass measurements is presently achieved with Penning traps where low-energy ions are stored and cooled [17, 18]. The combination of a trap system with a radioactive nuclear beam facility is realised with the ISOLTRAP at CERN [24, 25]. Masses of exotic nuclei have been determined with an accuracy of 10^{-7}.

In this paper we present a new experimental method for direct mass measurement [26] carried out at the GSI. We expected that this method will have several unique features and clear advantages because of following reasons.

- The heavy-ion synchrotron SIS can provide beams of all stable nuclides from protons up to uranium with maximum kinetic energies corresponding to a magnetic rigidity of 18 Tm [27]. The beams of relativistic exotic nuclei are produced in a reaction target by fragmentation or fission of the projectiles in peripheral nuclear collisions.

- In-flight separation of the projectile fragments with the fragment separator FRS provides nuclei with half-lives down to the sub–μs range independent of the chemical properties of the produced elements [28].

- A storage ring ESR [31] is a modern experimental facility of large acceptance. Consequently fragment beams can be injected with a high efficiency which permits mass measurements of very exotic species.

- A large number of different isotopes can be stored simultaneously. This is not only an advantage for calibration with known reference masses but also facilitates to investigate large areas of the nuclear chart in a systematic way.

- Each isotope can be stored in various ionic charge states which provide redundant measurements and allows to establish a consistent network of masses.

- We can use an electron cooling which reduces the relative velocity spread of the fragments to values of smaller than 10^{-6} such that their revolution frequencies are primarily determined by the ionic mass-to-charge ratio. The revolution frequencies can be obtained from the Fourier transform of the Schottky noise signal of the coasting beam [30].

We performed several pilot experiments with Schottky mass spectrometry at FRS-ESR in the light mass region [32, 33] and with fragmentation of gold [34]. All of them showed

that our expectations mentioned above have been proved true.
Here we present the results of large-scale direct mass measurements for neutron-deficient nuclides in the lead region using a ^{209}Bi projectile fragmentation and Schottky Mass Spectrometry (SMS). Only very few masses were known in this mass region (see Fig. ??). The first results have been published in [35] and have been presented in [36] and [37]. The results obtained in [35] covered an area of nuclides whose half-lives are longer than 10 s. This area has been chosen because it includes nuclides at the onset of α-radioactivity,which belong to the endpoints of known α-decay chains. The starting points of these long chains are very short-lived nuclides far off β-stability. Their masses were unknown and presently they cannot be measured directly via SMS because of their short half-lives. However, the combination of directly measured masses [35] with α-spectroscopy data allows to determine the masses of new nuclides and, hence, to extend the measured mass-surface considerably to the exotic region of nuclides beyond the proton drip-line.
From the new mass data which can be obtained in this way a variety of important topics are discussed [38].

1. The mass information for a new area of the chart of nuclides provides a challenging test for existing mass formulae and allows an examination of their predictive power.

2. The mass data allow to identify the proton drip-line in this mass region.

3. This also opens the possibility to identify nuclei that can undergo proton decay. The estimation of the proton radioactivity region becomes possible.

4. For even-even nuclides a more reliable prediction of the position of the two-proton drip-line can be given.

5. The existence of a Thomas-Ehrman shift in heavy nuclides can be tested by using the mass data obtained.

6. The mass-mapping of exotic nuclides in this region allows to study the strength of the Z=82 shell closure for nuclides far from β-stability.

This report presents the description of direct method of the mass measurement by using the Schottky mass spectrometry, the analysis of various approaches in determination of mass values and their uncertainties, the determination of masses within linked α-decay chains. In addition to the items discuused in [35] and [38] we present here the determination of masses for the isomeric states of exotic nuclides whose energies have been unknown so far. We have performed this determination by using the linked α-decay chains.

2 Experimental method

2.1 Production and separation of relativistic projectile fragments

In our experiment (see Fig. 2) the SIS has provided a beam of $^{209}Bi^{67+}$ ions with an energy of 930 MeV/u. Up to $5{\cdot}10^7$ ions per spill were extracted with fast extraction.

The beam was focused on an 8 g/cm^2 beryllium target placed at the entrance of the FRS. The primary beam and the projectile fragments emerged from the production

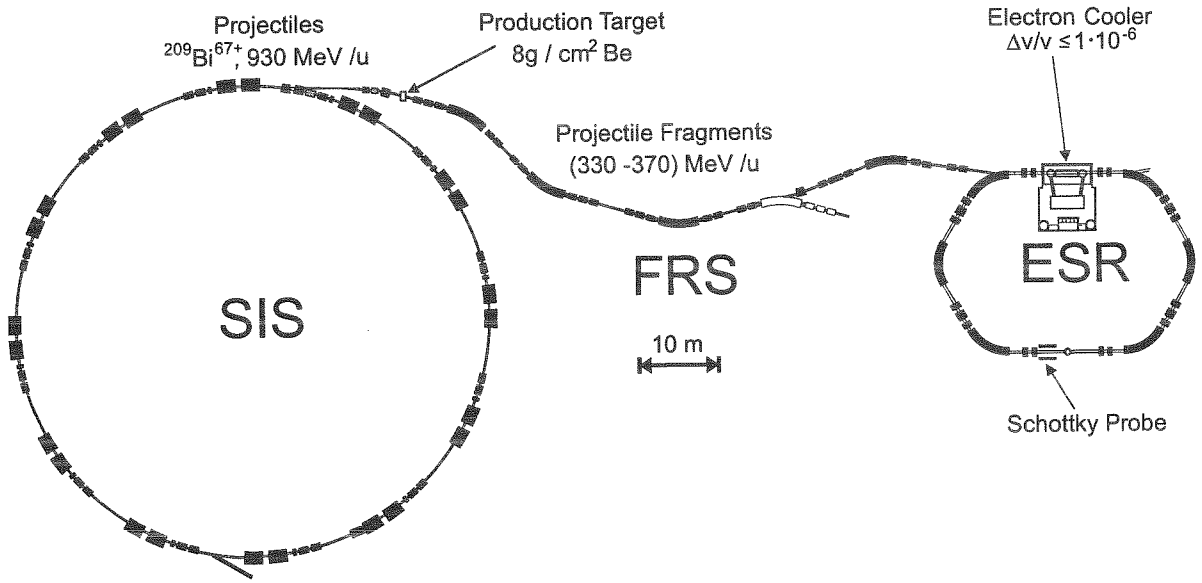

Figure 2: Layout of the high-energy facilities at GSI used for mass measurements of exotic nuclei.

target with kinetic energies of 330–370 MeV/u. At these energies the beam and the fragments carry only few electrons or are fully stripped behind the target.
The ionic charge state population of fragments emerging from the beryllium target is shown in Fig. 3 for a representative example. The abundance has been calculated with a model based on measurements at GSI and LBL [39]. Mainly bare, H-like, and He-like ions have been observed in accordance with the predictions of Fig. 3.
In principle, projectile fragmentation leads to all nuclei which can be generated by the removal of nucleons from the projectile, i.e., they can range from isotopes of the element of the projectile down to protons. However, the production cross-sections strongly decrease with the increasing number of removed nucleons. Reliable estimates of fragmentation cross-sections can be obtained from the semi-empirical parametrization implemented in the EPAX code [40]. The prediction for the formation cross sections of ^{209}Bi fragments in a beryllium target are presented as contour lines in the chart of nuclei, see Fig. 4. Furthermore, by nuclear charge-exchange reactions, also isotopes of the element above the projectile, here polonium nuclei, are abundantly produced. The FRS was used without an energy degrader in the dispersive mid focal plane. Thus all ions with the same magnetic rigidity were transmitted. The preparation and analysis of the experiment has been guided by computer simulations since the complex conditions including the ion-optical transmissions cannot be accurately estimated with pure analytical methods. For the calculation of the fragment distributions created in the production target and transmitted through the ion-optical systems the Monte-Carlo code MOCADI [41] is used. In the programme the cross sections characterizing the nuclear and atomic processes of the projectile–target interaction, the corresponding reaction kinematics, the atomic slowing down in matter, and the ion-optical properties of FRS and ESR are implemented.

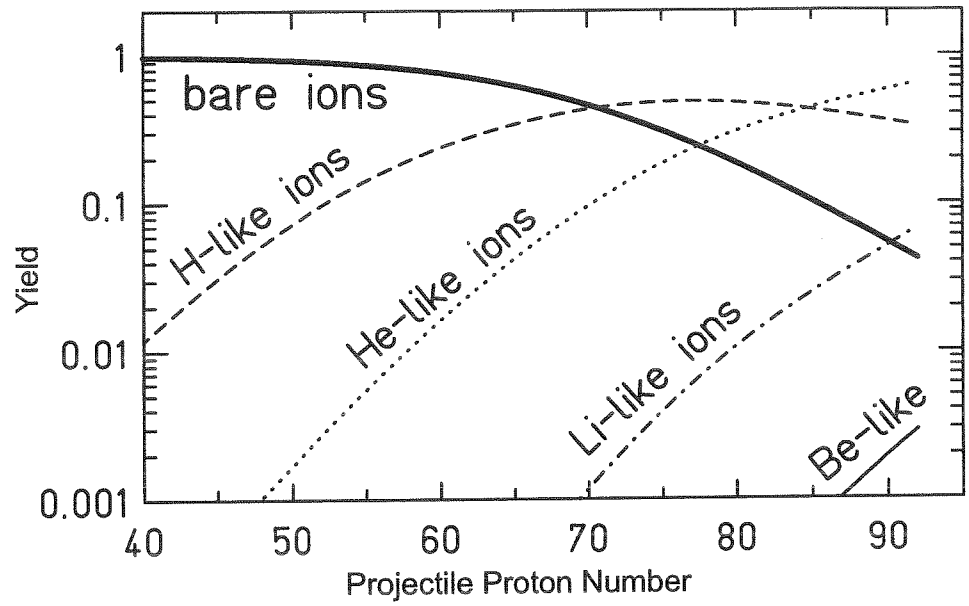

Figure 3: Calculated ionic charge state population of heavy ions [39] emerging from a beryllium target with velocities corresponding to a fixed magnetic rigidity of 6.7 Tm. Masses of stable nuclei were used in these calculations.

2.2 Injection, storage, and cooling of projectile fragments in the ESR

In Fig. 5 the important steps from the fragmentation process to the observed Schottky frequency-spectrum are presented as a result of such Monte-Carlo simulations. In the selected example the goal was to inject and to measure bare ^{197}Bi nuclei and all masses within the same $B\rho$-window.. To facilitate the understanding of the present example only bare bismuth isotopes are plotted for the $B\rho$ value of 6.7 Tm, though magnetic fields of the FRS and the ESR were both set to various magnetic rigidities in the experiment. The kinetic energy of the primary beam amounts to 930 MeV/u before the target and 350 MeV/u after the penetration of the target. The length of the bar for each Bi isotope corresponds to the FWHM of the velocity distribution. The $B\rho$ windows of ± 1 % for the transmission through the FRS and of ± 0.35 % for the injection acceptance of the ESR kicker magnet are indicated by full and dashed vertical lines respectively. Both areas are centered at the selected mean $B\rho$ value. Assuming that the kicker acceptance represents the limitation of the accepted phase space the enclosed isotopes can be stored in the ESR and cooled by merging an electron beam. The injected fragments are characterized by velocity distributions with widths of $\delta v/v \simeq 4 \cdot 10^{-3}$ (full lines). By electron cooling all ions are forced to the same mean velocity β_{cooler}. The resulting width of the distributions is $\delta v/v \simeq 7 \cdot 10^{-7}$. Due to the cooling, the fragments fully occupy the $B\rho$ acceptance of the ESR. The full circles denote species, which fall within the acceptance of the ESR, while the open dots denote ions whose magnetic rigidity after cooling is outside of the ESR storage acceptance. In reality the experimental conditions are more complex than illustrated in Fig. 5, i.e., we have a broad distribution of elements where the isotopes populate different ionic charge states, see Figure 3, and have wide velocity distributions depending on the A and Z difference to the primary beam. For optimum cooling conditions the number of stored ions and

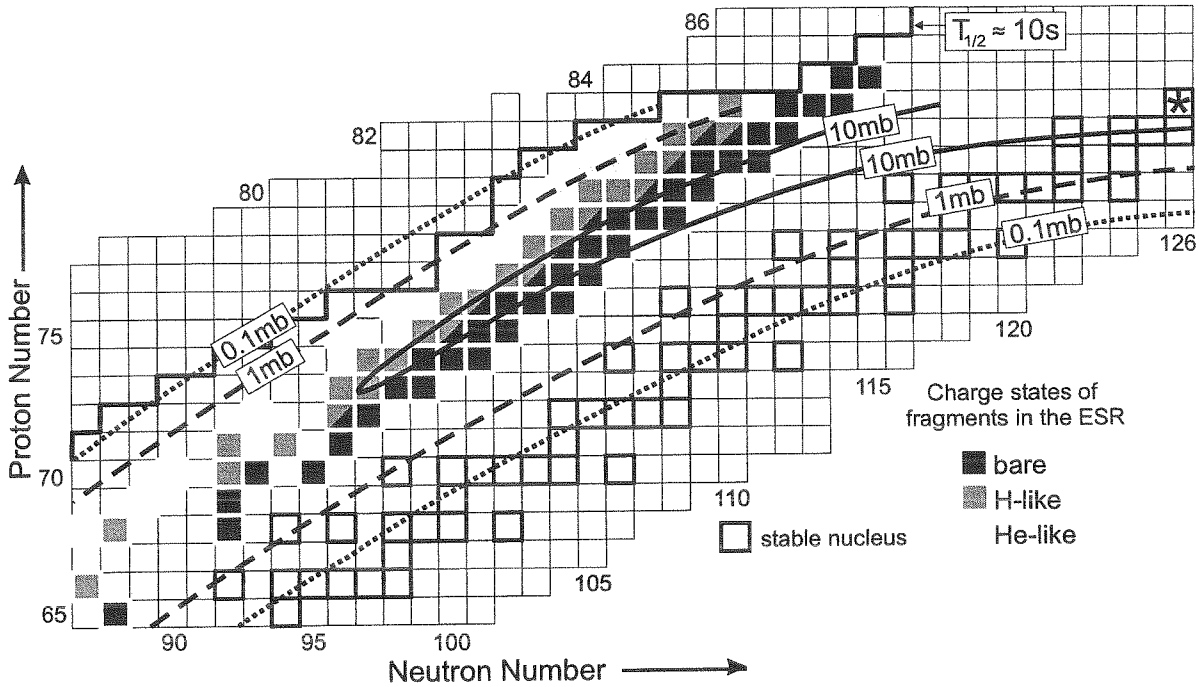

Figure 4: Production cross-sections [40] predicted for projectile fragmentation of ^{209}Bi projectiles in beryllium. The charge states of the fragments are indicated as recorded in the Schottky spectra at a $B\rho$ setting of 6.7 Tm. The helium-like and lithium-like ions approach the 10s-line, which at this time was a half-life limitation in our experiment.

the velocity of the cooler electrons have to be carefully selected. The cooling process contracts the phase space of the injected beams until a balance is reached between the cooling force and the intra-beam scattering due to Coulomb interaction between the stored ions. The equilibrium momentum spread depends critically on the number n of stored ions. At particle numbers of $n \geq 10^4$ ions, the relative momentum spread of the cooled beam increases as $\delta p/p \propto n^{1/3}$. However, for low-intensity beams with particle numbers $n \lesssim 5 \cdot 10^3$, a suppression of the intra-beam scattering is observed [30], and thus a velocity spread corresponding to $\delta p/p \lesssim 7 \cdot 10^{-7}$ is achieved by electron cooling. This condition improves the mass resolving power and therefore the intensity must be kept quite low.
The cooling time is roughly proportional to the third power of the velocity difference between the electron beam and the fragments to be cooled. With electron densities of typically $3{\cdot}10^6/\mathrm{cm}^3$, corresponding to a cooler current of about 200 mA along a 2 m straight section, most of the "hot" fragment beams can be cooled in about 30 s. In order to measure fragments with shorter half-lives, the velocity of the cooler electrons was chosen to be close to the mean velocity of the desired fragments. By this method nuclei with half-lives of $T_{1/2} \geq$10 s have been cooled and have been observed in the frequency spectra.

2.3 Schottky mass spectrometry

At each turn, the stored ions, circulating in the ESR with revolution frequencies of about 2 MHz, induce a mirror charge on electrostatic pick-up electrodes installed in

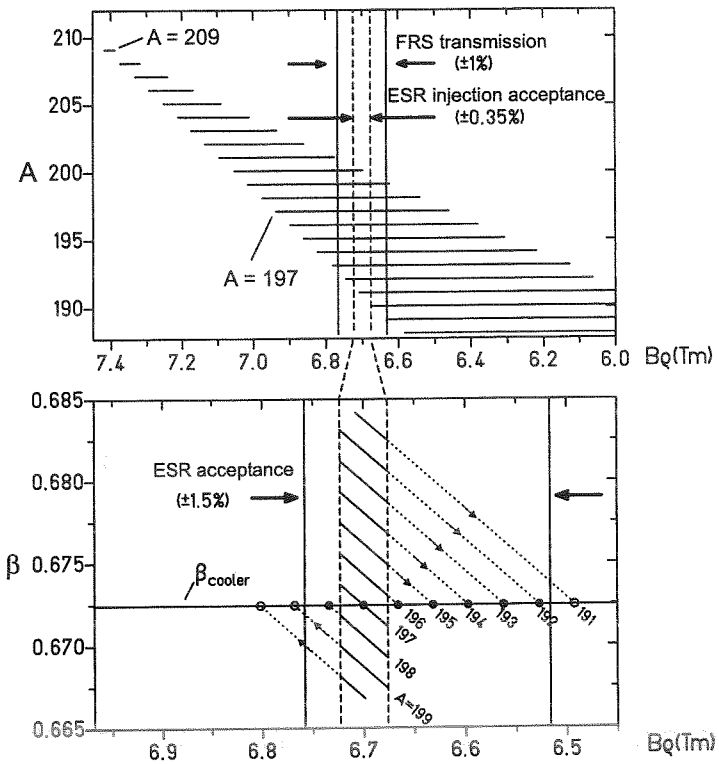

Figure 5: Scheme of production, separation and cooling of bare bismuth fragments illustrated in the $B\rho$ space. Upper part: Calculated magnetic-rigidity distributions of bismuth isotopes at the exit of the 8 g/cm^2 beryllium target. Lower part: Velocity spread (in units of the velocity of light $\beta = v/c$) as a function of the magnetic rigidity of the stored and cooled bismuth fragments. The injected fragments are characterized by incident velocity distributions with widths of $\delta v/v \simeq 4 \cdot 10^{-3}$ (slanting full lines).

the ring. Each species of the circulating multi-component ion beam has its own mean revolution-frequency $f_i = v_i/C_i$, with v_i and C_i being its velocity and length of its closed orbit, respectively. A typical orbit lenght in the ESR is $C = 108.4$ m. As C_i depends on the mass-to-charge ratio $(m/q)_i$, we obtain to first order for two species (index i, j) the relative frequency difference:

$$\frac{f_i - f_j}{f_i} = -\alpha_p \cdot \frac{(m/q)_i - (m/q)_j}{(m/q)_i} \tag{1}$$

where $\alpha_p = dC/C/(d(B\rho)/(B\rho))$ is the momentum compaction factor. This ion-optical parameter characterizing the relative variation of the orbital length C per relative variation of the magnetic rigidity $B\rho$ has a value of approximately 0.14 in our experiment. The width of a frequency distribution is determined by the width of the velocity distribution of a selected fragment:

$$\frac{\delta f_i}{f_i} = \left(\frac{1}{{\gamma_i}^2} - \alpha_p\right) \cdot {\gamma_i}^2 \cdot \frac{\delta v_i}{v_i} \tag{2}$$

where γ_i represents the relativistic Lorentz factor and $\delta v_i/v_i$ is the relative width of the velocity distribution for a selected fragment. When the ions are cooled they are

forced to the same mean velocity with a small velocity spread thus their frequency distributions become narrow and a high mass resolving power can be achieved.
Equations (1) and (2) are the basis for the Schottky Mass Spectrometry (SMS). If α_p and the mass-to-charge ratio of a reference ion are precisely known, unknown masses can be determined by application of Eq. (1). Generally also α_p is obtained by means of Eq. (1) using the lines of ions with well known m/q values. The mean values of the frequency distributions $f_{i,j}$ represent the main observables of SMS. The mass resolving power R_m is given by:

$$R_m = \left| -\alpha_p \cdot \frac{f}{\delta f} \right| = \left(\frac{\alpha_p}{1 - \gamma^2 \alpha_p} \right) \cdot \frac{v}{\delta v} \tag{3}$$

for $1/\gamma^2 > \alpha_p$ This equation shows that the reduction of the velocity spread $\delta v/v$ is crucial for achieving a high mass-resolving-power. For example, the mass resolving power for a 350 MeV/u uncooled fragment beam would be only about 50, however, we achieved with cooled beams in our experiment a mass resolving power of 350000.
Schottky noise spectroscopy [42] is widely used for non-destructive beam diagnosis in circular accelerators and storage rings. Signals induced by the stored circulating ions in probes are recorded and analyzed. Already in our pilot experiments with cooled projectile fragments [32, 33] we have applied Schottky diagnostics. Since then, we have gradually improved this technique for the requirements of precise mass spectrometry [34, 36, 43, 44, 45, 46].
In the experiment, due to technical reasons the Schottky noise signal of the 16^{th} harmonic of the revolution frequency was analyzed. After amplification and down-mixing by a suitable rf-frequency of typically 30 MHz provided by a local oscillator, small frequency bands of 10 kHz or 100 kHz were selected depending on the needed frequency resolution. The bandwidth of 100 kHz covers a large part of the orbits allowed by the ESR $B\rho$-acceptance. These low-frequency bands were sampled for 160 ms and 16 ms, respectively, and Fourier analyzed by real-time fast Fourier transformation (FFT) with 1601 frequency channels. Subsequently up to 10^4 samples were averaged in order to achieve sufficient signal-to-noise ratio even for low particle numbers. A low-resolution 100-kHz spectrum is shown in the upper part of Fig. 6. In this example, the magnetic rigidity of the FRS and of the ESR and the voltage of the electron cooler (U = 181 kV) and its electron current (I = 250 mA) were set to optimize the transmission and the cooling of fragments with mass-to-charge ratios of about 2.35. The spectrum contains about 90 different nuclear species in bare, hydrogen-like, or helium-like charge states as presented in Fig. 4. However, isobaric triplets characterized by equal A and q, cannot be resolved in such a 100-kHz broadband spectrum. The necessary frequency resolution is obtained in the 10-kHz spectra. Only these spectra were used for the mass determination. As an example, such a high-resolution spectrum is displayed in the lower part of Fig 6. The spectrum is an average of 1000 single FFT-spectra and recorded under the same conditions as the 100-kHz spectrum in Fig. 6. The isobars with the same ionic charge states are clearly resolved [43]. Depending on the charge of the ions often less than 10 particles were necessary to detect the revolution frequency of an isotope. This sensitivity requires about 1000 averages for a 10-kHz FFT spectrum, where each average took 160 ms. The identification of the peaks in the Schottky spectra has been performed by a computer assisted peak pattern comparison [36]. In this procedure the known atomic masses of nuclides from ref. [12] were corrected for the missing electrons

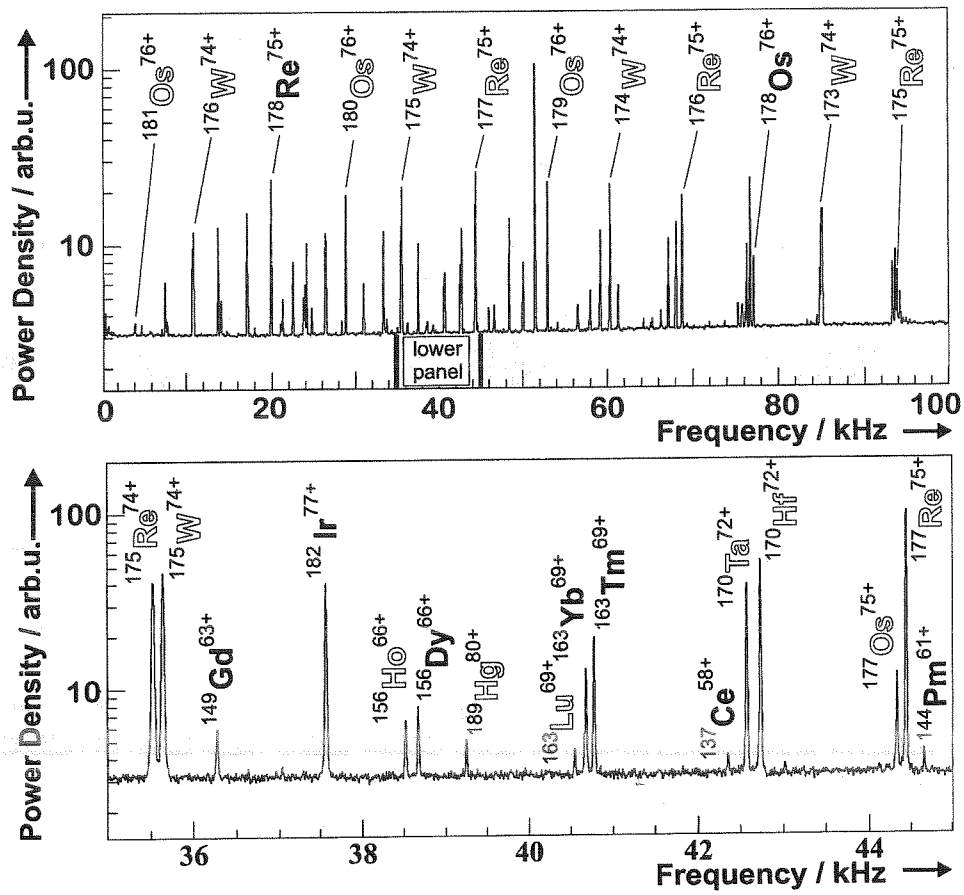

Figure 6: Schottky frequency spectra. Upper panel: Low-resolution (100-kHz bandwidth) Schottky spectrum of stored and cooled fragments measured for 160 s at a $B\rho$ setting of 7.1 Tm. The frequency scale denotes the difference between the 16^{th} harmonic of the revolution frequency and an admixed external frequency of 30.700 MHz. Lower panel: High-resolution (10-kHz bandwidth) Schottky-spectrum. Most of the frequency lines split up into isobaric doublets or triplets characterized by the same ionic charge. The peaks of ions with known masses used for calibration are indicated by bold letters; nuclei with previously unknown masses are indicated by outlined letters.

and for the electron binding energies [47, 48, 49]. Based on the input values of the cooler voltage, the momentum compaction factor α_p, and the local oscillator frequency a 100-kHz frequency spectrum was generated with those masses which were expected from Monte-Carlo simulation to enter into the ESR. After the peak pattern of the 100-kHz spectra was identified, high-resolution spectra with a bandwidth of 10-kHz were recorded and the identification was verified. Depending on the charge of the ions often less than 10 particles were necessary to detect the revolution frequency of an isotope. This sensitivity requires about 1000 averages for a 10-kHz FFT spectrum, where each average took 160 ms.

Including the time for electron cooling in addition we were able to access nuclei with effective half-lives longer than 10 s. This holds for nuclear decay modes which are independent of the number of bound electrons.

3 The mass evaluation

In total about 12000 frequency peaks in about 1100 spectra with a bandwidth of 10 kHz were investigated. Different methods of analysis of the Schottky frequency spectra [34, 36, 37] have been employed to extract and to check the mass values. In all these methods we used the assumptions that the dependence of the mass-to-charge ratio on the frequency is described by a first order polynomial and that all references used are not contaminated by isomeric states.
In a first step of data analysis the mass values were determined by using the known masses as a reference in a linear regression. The nonlinearity of α_p as a function of frequency required a calibration for each 10-kHz spectrum. Afterwards the mass value obtained for each isotope was corrected for its charge state and the results for each isotope were averaged. The total uncertainties range from 50 keV, and for very few cases, up to several 100 keV.
The mass values determined by this conventional method are in good agreement with the results obtained by a general correlation analysis.
In this general approach a maximum likelihood method [50] has been applied in the evaluation of the masses and their errors.
This section is devoted to discreption of different methods of analysis of raw experimental data and to comparison of mass values which have been obtained by these methods. We will start with the general approach.

3.1 The general approach

3.1.1 The basic equations

In the following the index j represents a specific Schottky spectrum, which consists of frequency peaks. Each peak denoted by μ corresponds to an isotope in a specific charge state. The mass-to-charge ratio deviates randomly from the linear calibration ansatz. The difference is a statistical variable with a mean value equal to zero and a standard deviation Δ_j^μ.

$$\frac{M_j^\mu}{q_j^\mu} - a_j^0 - a_j^1 x_j^\mu = l_j^\mu \pm \Delta_j^\mu. \tag{4}$$

M_j^μ and q_j^μ represent the mass and charge state of the ion connected with the frequency peak x_j^μ. In a good approximation the statistical variable l_j^μ has a Gaussian distribution with a width proportional to standard deviation $\sigma_{x_j^\mu}$ of the frequency peak

$$\Delta_j^\mu = s\sigma_{x_j^\mu}. \tag{5}$$

The scaling factor s is unknown and can be deduced from the maximum likelihood condition (14). For known masses quoted with an accuracy [12] $\Delta\tilde{M}_\gamma$ we assume:

$$M_\gamma^b - \tilde{M}_\gamma^b = l_\gamma \pm \Delta\tilde{M}_\gamma, \tag{6}$$

where $\tilde{M}_\gamma^b$ denotes a known mass from [12] of a bare nuclide and M_γ^b is the mass of the same isotope determined by SMS. l_γ is the statistical variable with a mean value equal to zero forming a Gaussian distribution. The masses and the Q-values in the α-decay chain are related by:

$$M_\alpha^m - M_\alpha^d - m_\alpha - \tilde{Q}_\alpha^b = l_\alpha \pm \Delta\tilde{Q}_\alpha, \tag{7}$$

where M_α^m, M_α^d are two bare nuclides (mother and daughter) characterized by the energy $\tilde{Q}_\alpha^b$ taking into account the differences of bare and neutral atoms involved, determined with an accuracy of $\Delta\tilde{Q}_\alpha$. m_α is the mass of the α particle and l_α is again the statistical variable with mean value equals zero and Gaussian distribution. The Gaussian distribution is defined by the expression:

$$f(l,\sigma) = \frac{1}{\sqrt{2\pi}\sigma} \exp\left[-\frac{l^2}{2\sigma^2}\right]. \tag{8}$$

The method of maximum likelihood consists of estimating the set of masses, coefficients of the calibration curve and the scaling factor, which maximize the joint probability density function L. The global likelihood function L can be written as

$$L = L_c \cdot L_{EXP}. \tag{9}$$

The "experimental" part of the likelihood function, denoted by L_{EXP}, is defined as follows:

$$L_{EXP} = \prod_{j,\mu} f(l_j^\mu, \Delta_j^\mu), \tag{10}$$

where j enumerates the spectra and the index μ runs over all peaks within a given spectrum j.
The calibration term L_c of the likelihood function has the form

$$L_c = \prod_\gamma f(l_\gamma, \Delta\tilde{M}_\gamma) \prod_\alpha f(l_\alpha, \Delta\tilde{Q}_\alpha), \tag{11}$$

where γ runs over reference nuclides with known masses and α runs over α-decay chains with measured Q_α values.
The maximum of the global likelihood function L, as a function of the masses M_μ^b, the coefficients of the calibration curve a_j^k and the scaling factor s can be found by solving the equations

$$\frac{\partial \ln L}{\partial a_j^k} = 0 \qquad k = 0,1\,;\ j = 1,2,\ldots,N_S, \tag{12}$$

$$\frac{\partial \ln L}{\partial M_\mu^b} = 0 \qquad \mu = 1,2,\ldots,N_n, \tag{13}$$

$$\frac{\partial \ln L}{\partial s} = 0. \tag{14}$$

Here, N_S and N_n denote the number of used spectra and the number of different nuclides, respectively. The index k enumerates the polynomial coefficients.

3.1.2 Solution of the basic equations

The solution of eq. (12) yields the two unknown polynomial coefficients for every spectrum j:

$$\hat{\mathbf{A}}_j \begin{pmatrix} a_j^0 \\ a_j^1 \end{pmatrix} = \sum_\mu w_j^\mu \frac{M_j^\mu}{q_j^\mu} \begin{pmatrix} 1 \\ x_j^\mu \end{pmatrix}, \tag{15}$$

where

$$w_j^\mu = \frac{1}{\Delta_j^{\mu 2}} = \frac{1}{s^2 \sigma^2_{x_\mu^j}} \tag{16}$$

and

$$\hat{\mathbf{A}}_j = \begin{pmatrix} \sum_\mu w_j^\mu & \sum_\mu w_j^\mu x_j^\mu \\ \sum_\mu w_j^\mu x_j^\mu & \sum_\mu w_j^\mu \left(x_j^\mu\right)^2 \end{pmatrix}. \tag{17}$$

The sum $\sum_\mu$ in the matrix $\hat{\mathbf{A}}_j$ and on the right-hand side of eq. (15) runs over all peaks in the spectrum denoted by the index j.
The coefficients a_j^0 and a_j^1 can be calculated from the formula

$$\begin{pmatrix} a_j^0 \\ a_j^1 \end{pmatrix} = \hat{\mathbf{A}}_j^{-1} \sum_\mu w_j^\mu \frac{M_j^\mu}{q_j^\mu} \begin{pmatrix} 1 \\ x_j^\mu \end{pmatrix}, \tag{18}$$

where

$$\hat{\mathbf{A}}_j^{-1} = \frac{1}{\det(\hat{\mathbf{A}}_j)} \begin{pmatrix} \sum_\mu w_j^\mu \left(x_j^\mu\right)^2 & -\sum_\mu w_j^\mu x_j^\mu \\ -\sum_\mu w_j^\mu x_j^\mu & \sum_\mu w_j^\mu \end{pmatrix}. \tag{19}$$

The mass of an ion M_j^μ is equal to the mass of the bare nucleus M_μ^b plus the mass of the bound electrons E_j^μ. Thus, we can write

$$M_j^\mu = M_\mu^b + E_j^\mu. \tag{20}$$

The equation (13) for the mass M_μ^b has the form

$$\sum_j w_j^\mu \frac{M_j^\mu}{\left(q_j^\mu\right)^2} - \sum_j w_j^\mu \frac{\hat{f}_j\left(x_j^\mu\right)}{q_j^\mu} - \frac{\partial ln L_c}{\partial M_\mu^b} = 0, \tag{21}$$

where the sum $\sum_j$ runs over all spectra in which the nuclide appears. This implies that we have as many equations (21) as different nuclides.
The value of the function $\hat{f}_j$ at x_j^μ can be written in the form

$$\hat{f}_j\left(x_j^\mu\right) = a_j^0 + a_j^1 x_j^\mu = \left(1, x_j^\mu\right) \begin{pmatrix} a_j^0 \\ a_j^1 \end{pmatrix}. \tag{22}$$

The last expression (22), together with equations (18) and (21) gives us the final set of equations for the mass values

$$\sum_j \frac{M_j^\mu w_j^\mu}{\left(q_j^\mu\right)^2} - \sum_{j,\beta} \frac{w_j^\mu}{q_j^\mu} \left[\left(1, x_j^\mu\right) \hat{\mathbf{A}}_j^{-1} \begin{pmatrix} 1 \\ x_j^\beta \end{pmatrix} \frac{w_j^\beta M_j^\beta}{q_j^\beta} \right] - \frac{\partial ln L_c}{\partial M_\mu^b} = 0. \tag{23}$$

Here, the index j denotes the spectrum in which the nuclide M_μ^j occurs and the index β runs over all nuclides within the spectrum labeled by j. The equation (23) may be written symbolically

$$\mathbf{W} \vec{M}^b = \vec{w}. \tag{24}$$

Here, the symmetric matrix $\mathbf{W}$ has the dimensions $N_n \times N_n$, where N_n denotes the number of nuclides. The elements of the matrix $\mathbf{W}$ have the form:

$$W_{\mu\mu} = \sum_j \frac{w_j^\mu}{\left(q_j^\mu\right)^2}\left[1 - w_j^\mu \left(1, x_j^\mu\right) \hat{\mathbf{A}}_j^{-1} \begin{pmatrix} 1 \\ x_j^\mu \end{pmatrix}\right] + \frac{1}{\left(\Delta\tilde{M}_\mu\right)^2} + \frac{1}{\left(\Delta\tilde{Q}_\alpha^\mu\right)^2}, \tag{25}$$

$$W_{\mu\nu} = -\sum_j \left[\frac{w_j^\mu w_j^\nu}{q_j^\mu q_j^\nu}\left(1, x_j^\mu\right) \hat{\mathbf{A}}_j^{-1} \begin{pmatrix} 1 \\ x_j^\nu \end{pmatrix}\right] - \frac{1}{(\Delta\tilde{Q}_\alpha^\nu)^2}, \qquad \text{for } \mu \neq \nu. \tag{26}$$

$$\tag{27}$$

The vector $\vec{w}$ can be written as

$$w_\mu = \frac{\tilde{M}_\mu^b}{\left(\Delta\tilde{M}_\mu\right)^2} \pm \frac{m_\alpha + \tilde{Q}_\alpha^b}{\left(\Delta\tilde{Q}_\alpha\right)^2} + B_\mu, \tag{28}$$

where the first term is added when the $\tilde{M}_\mu^b$ is mass of a reference nuclide, the second term has a plus sign if the nuclide is a mother nucleus in the α-decay chain and a minus sign if it is a daughter. The last term is

$$B_\mu = \sum_{j,\beta} \frac{w_j^\mu w_j^\beta}{q_j^\mu q_j^\beta}\left(1, x_j^\mu\right) \hat{\mathbf{A}}_j^{-1} \begin{pmatrix} 1 \\ x_j^\beta \end{pmatrix} E_j^\beta - \sum_j \frac{w_j^\mu E_j^\mu}{\left(q_j^\mu\right)^2}. \tag{29}$$

The equation (14) has been used for the determination of the scaling parameter s

$$\frac{1}{N_n} \cdot \sum_{j,\mu} \frac{l_j^{\mu 2}}{\sigma_{x_j^\mu}^2} = s^2. \tag{30}$$

The equations (24) and (30) have been solved iteratively and convergence has been reached after 8 steps. The scaling parameter s has been found to be equal to 0.000163 u kHz^{-1}e $^{-1}$.

3.1.3 Error Estimation

For each nuclide with the index μ and the mass M_μ^b the diagonal elements of the inverse matrix $\mathbf{W}^{-1}$ have been used to determine the statistical error:

$$\left(\sigma_{M_\mu^b}^{stat}\right)^2 = \mathbf{W}^{-1}{}_{\mu\mu}, \tag{31}$$

This error includes the uncertainties from the reference nuclei and from the Q_α-values [12, 13], used for the determination of the mass under investigation as well as the errors in the frequency determination and the number of measurements for each isotope. The result is that the statistical error is approximately a few ten keV for nuclei which are linked to numerous reference nuclei whereas up to 200 keV appears for very few unfavorable cases (see Tab. 4).
The systematic error has been estimated in a separate evaluation. Only those reference nuclides with mass uncertainties of less than 30μu [12] (82 isotopes) (see Tab. 5) were used for calibration in this investigation. The goal was to determine the masses of the reference nuclei characterized by a mass uncertainty of larger than 30μu [12] ($N_k = 28$

isotopes). A comparison of these mass values M_γ^b with their corresponding tabulated values $\tilde{M}_\gamma^b$ [12] led to a systematic error of σ^{syst}=100 μu derived with the following equation:

$$\sum_\gamma \frac{\left(M_\gamma^b - \tilde{M}_\gamma^b\right)^2}{\left(\Delta\tilde{M}_\gamma^b\right)^2 + (\sigma^{syst})^2 + (\sigma_\gamma^{stat})^2} = N_k, \tag{32}$$

In the analysis of the data it was observed that neighboring frequency peaks with a distance closer than about 90 Hz cause correlated deviations from the mass-to-charge ratio deduced from the calibration curve. Such deviations for all the reference nuclei are plotted in Fig. 7 for their nearest neighboring frequency peaks. The correlation for those peaks with a relative distance of less than 90 Hz is clearly seen, therefore, those peaks have been discarded from our mass analysis. In spite of this selection residual frequency shifts are assumed to be a major reason for the systematic error in our measurement. The frequency shifts are similar to the cyclotron frequency shifts in Penning traps [51]. Due to a high number of ions circulating with close distances next to each other in the ESR, Coulomb interactions may lead to collective coupled motions.
The results of our general maximum likelihood method is in good agreement with other preceding methods (see below) of mass evaluation [36, 43] of the same experiment, where different calibration procedures and selection criteria were applied.

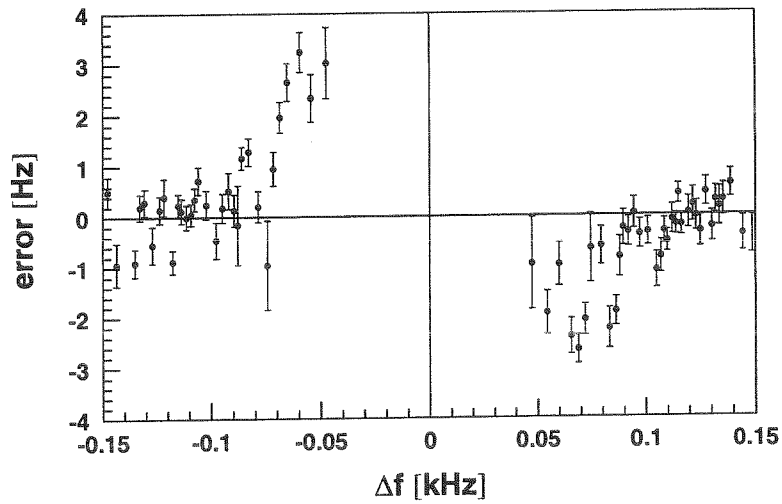

Figure 7: Deviations of the mass-over-charge ratio from the calibration curve versus the distance to the nearest neighboring frequency peak. The distance is assumed positive for a particle on an inner trajectory The closed circles and the error bars represent the mean value and the width for an ensemble of 100 mass-over-charge deviations.

3.2 Other methods of mass evaluation

The mass values measured directly have been obtained by data handling of information obtained during the experimental run with small preselection of parts of the spectra mentioned in the previous subsection. This block of information contains the repeated

measurements for various fixed m/q values (so called "cuts") and within the "cuts" for various 10-kHz spectra, which have been performed with different sets of local oscillator, cooler voltage and current in the electron cooler. All this provided different experimental conditions for various spectra measured. We observed in our spectra a peak-broadening of different widths, peak shifts and a non constant background.
Thus, the same nuclide appears in various spectra which are different in their "structure" and quality. Moreover the number of spectra in which one nuclide has been identified changes from 1 to 180. Table 1 shows the number of spectra in which the same nuclide has been observed in different charge states (from "bare" ($0e^-$) to lithium-like ($3e^-$)). Therefore it is obvious to expect a large scattering of statistical error bars for different nuclides.

To confirm the results of our general method of analysis and to clarify the problem of error bars we present below the results of other types of the analysis based on the careful selection of raw data.
The main idea of this analysis was to exclude spectra with peak broadening, visible peak shifts, non constant background, with irregularities in the α_p-behaviour and those which were recorded immediately after the injection into the ESR. Thus, we have choosen the "basic" data which have only been used in the further analysis. These data contains about a sixth part of full information obtained.
The additional analysis with these "basic"data have been performed by two methods. Both methods of analysis used are based on the assumption of strong linearity of m/q-values versus the frequency, which is only some approximation. The experimental values were fitted by the formula $m/q = a + bf$,where a and b are the parameters of intercept and slope of straight line respectively. The first method of analysis applies the least square procedure in each individual 10-kHz spectrum,
As the error bars for frequencies are not exceedingly small in comparison to m/q the linear regression with two dimensional error bars should be used (so called, confluent analysis) [52]. The χ^2-merit function which have to be minimized is:

$$\chi^2(a,b) = \sum_{i=1}^{N} \frac{\Big((m/q)_i - a - bf_i\Big)^2}{\sigma^2_{(m/q)_i} + b^2 \cdot \sigma^2_{f_i}}, \tag{33}$$

where N is the number of peaks in 10-kHz spectrum fitted and $\sigma_{(m/q)_i}$ and σ_{f_i} are, respectively, the m/q and f-standart deviations for the i-th point.
We have used the iteration procedure to minimize this equation with respect to parameters a and b. We started with general one-dimensional error procedure to minimize χ^2 with respect to slope parameter b. The value of b which leads to saturation in minimization after R iterations and gives the minimum with respect to a was choosen as a final. Practically the saturation points were reached after a very few steps.
The next and more deeply selected procedure of data handling was named "two peak analysis". To elaborate the criteria which could be useful for the "two peak" analysis we investigated carefully the spectra belonging to the m/q "cuts" which are more close to the beta-stability line and which contain the nuclides with known masses. All possible combinations of two peaks with known mass values (having no long lived isomeric states) are taken to determine the α_p . With the α_p obtained for each spectrum the unknown mass-values can be determined if they match with the following criteria:

Table 1: Number of spectra in which the nuclides appeared in different ionic charge states. $0e^-$ represents "bare nuclides", whereas $1e^-$, $2e^-$ and $3e^-$ hydrogen-like, helium-like and lithium-like ions, respectively.

El.	Z	N	A	Charge states				El.	Z	N	A	Charge states			
				$0e^-$	$1e^-$	$2e^-$	$3e^-$					$0e^-$	$1e^-$	$2e^-$	$3e^-$
La	57	76	133	1				W	74	96	170		3	7	1
Ce	58	76	134		1				74	97	171		14	20	
Nd	60	75	135			2			74	98	172	7	28	5	
	60	78	138			1			74	99	173	3	64		
Pm	61	77	138			3			74	100	174	42	48	11	1
Ho	67	89	156	2	16	3			74	101	175	74	37	2	
Er	68	90	158	8	13	2			74	102	176	40	13	3	
Tm	69	89	158			4			74	103	177	2	4	1	
	69	91	160		4			Re	75	97	172			1	
Yb	70	90	160			4			75	98	173			20	
	70	91	161		6	5			75	99	174	5	36	27	
	70	92	162		5	16			75	100	175	30	80	28	
	70	94	164	14	29	2			75	101	176	5	2	9	
Lu	71	91	162			2			75	102	177	85	28	7	
	71	92	163		7	7			75	103	178	14	7	2	
	71	93	164		10	8		Os	76	98	174			11	
	71	95	166		16	1			76	99	175		9	18	
Hf	72	92	164			1	3		76	100	176			1	1
	72	93	165			3			76	101	177	35	73	15	
	72	94	166			12	1		76	102	178	33	41	6	
	72	95	167		9				76	103	179	74	22	5	
	72	96	168	28	40	17			76	104	180	93	86		
	72	98	170	49	30				76	105	181	52	16	2	1
	72	99	171	54	9	1		Ir	77	100	177		1	10	1
Ta	73	94	167			3			77	101	178		5	10	
	73	95	168		13	7			77	102	179	11	50	32	2
	73	96	169		15	20			77	103	180	2	41	20	
	73	97	170	25	47	7			77	104	181	38	72	31	
	73	98	171	27	84	12			77	106	183	85	27	7	
	73	100	173	47	5	3			77	107	184	1	9		
	73	102	175	1	3				77	108	185	4	7	2	

El.	Z	N	A	Charge states				El.	Z	N	A	Charge states			
				$0e^-$	$1e^-$	$2e^-$	$3e^-$					$0e^-$	$1e^-$	$2e^-$	$3e^-$
Pt	78	100	178			2		Tl	81	110	191	(68	69	32	1)
	78	101	179			16			81	111	192	12	49	14	
	78	102	180		3	3	5		81	112	193	(79	8	1)	
	78	103	181	4	21	34			81	113	194	6	11	6	
	78	104	182	27	17	1			81	114	195	38	10		
	78	105	183	(19	89	29)		Pb	82	106	188			1	1
	78	106	184	81	46	1			82	107	189			(9)	
	78	107	185	(126	12	11)			82	108	190		7	12	
	78	109	187	16	9	1			82	109	191	25	61	56	4
Au	79	102	181			2			82	110	192	25	28	7	
	79	103	182		1	11			82	111	193	52	77	23	1
	79	104	183		17	44	3		82	112	194	77	7	1	1
	79	105	184	31	48	26			82	113	195	76	40	20	
	79	106	185	(25	119	7)			82	114	196	61	7	2	
	79	108	187	(74	31	6)			82	115	197	14	2	4	
	79	109	188	7	34	12			82	116	198	30	11		
	79	110	189	23	2			Bi	83	109	192		1	3	
Hg	80	104	184		4	9	1		83	110	193	1	22	14	
	80	105	185		(18	41)			83	111	194		58	15	
	80	106	186	10					83	112	195	17	75	17	
	80	107	187	1	63	82			83	113	196	84	62	20	
	80	108	188	36	37				83	114	197	94	35	12	
	80	109	189	86	27	12			83	115	198	48	25	10	
	80	110	190	122	34	2		Po	84	113	197		3		
	80	112	192	90	9	3			84	114	198	18	2		
Tl	81	105	186			(5)			84	115	199	35	53		
	81	106	187			(18)			84	116	200	49	2		
	81	107	188	6	17	17	3		84	117	201	56	20	1	
	81	108	189	(28	74	50	1)		84	118	202	28	5	2	
	81	109	190	13	87	12									

- $|0.1405 - \alpha_p| \leq 0.0025$
- $|f_{ref_1} - f_{ref_2}| \geq 2 \cdot min(|f_{ref_1} - f_{unknown}|, |f_{ref_2} - f_{unknown}|)$.

An additional statistical criterion was added in order to get rid of the statistical outlyers: $|m_i - \overline{m}| \leq 2 \cdot \sqrt{(\Delta m_i)^2 + (\Delta \overline{m})^2}$,
$\overline{m}$ means the arithmetical mean value and m_i stands here for the largest deviation from the arithmetical mean value. In this way the outlyers are detected and they are removed. After this all masses and errors - up to this part ionic- are converted to atomic masses. Atomic masses which belong to a given nuclide are averaged. The masses are averaged with the weights of the errors and for the uncertainty the maximum of either the weighted error or the scattered error is taken. Finally the masses are compared with the experimental values if they were measured previously [13] to obtain an additional systematical error which turned out to be 55 μu. This systematical error is due to uncertainties which we could not detect or which we were not able to correct for. So finally every error bar is quadratically enlargened by 55 μu.
As it was expected the error bars obtained by the two mentioned methods ranges from $\simeq$ 50 keV up to a few hundred keV.
The comparison of mass values obtained by the three methods of analysis performed in this article is presented in Fig.8 for one typical part of the data. A satisfactory agreement between the mass values can be seen.

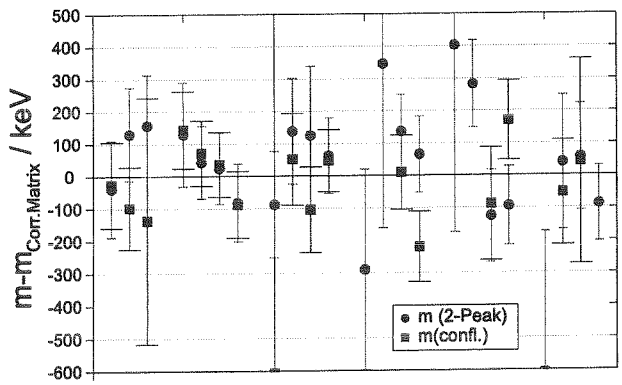

Figure 8: Comparison of the mass values obtained by various methods of analysis. $m_{Corr.Matrix}$ refers to the results of general analysis (subsection 3.1)

3.3 Mass evaluation within α-decay chains

As it was mentioned above, the results obtained by Schottky mass-spectrometry covers an area of nuclides at the onset of α-radioactivity, which belong to the endpoints of known α-decay chains. The starting points of these long chains are very short-lived nuclides far off β-stability. The masses of most nuclides in the chains and especially for the nuclides at the top of chains cannot be measured directly via SMS because of their very short half-lives. However, the combination of α-spectroscopy data with our directly measured masses allows to determine the masses of new nuclides and, hence, to extend the measured mass-surface considerably to the exotic region of nuclides beyond

the proton drip-line.

Table 2 presents the list of nuclides in the mass region A $\approx$ 150 - 218 which are completely linked by α-transitions.
In the first column the nuclides on the ends of the α-decay chains are given. Their masses have been measured directly by Schottky spectrometry . The half-lives of these nuclides are shown in parenthesis. The second column of Table 2 contains all the nuclides including their half-lives which are linked by α-decay chains with the end-nuclide. Some of them (marked by bold letters) have also been measured directly provided their half-lives were longer than 10 s –the typical minimim time necessary for beam cooling.
If the atomic mass value for one nuclide (Z, A) in an α-decay chain is known, then the mass value of the i-th member of the chain can be written as:

$$M(Z+2i, A+4i)c^2 = M(Z,A)c^2 + \sum_{k=1}^{i} Q_{\alpha k} + iM(^4He)c^2. \qquad (34)$$

Here Q_{α_k} is the energy of the k-th transition in the chain which is equal to $Q_{\alpha k} = E_{\alpha k} \cdot A_k/(A_k - 4)$ and $E_{\alpha k}$ is the kinetic energy of the corresponding α-particles. In cases where excited states in either the mother or daughter nucleus are involved the corresponding excitation energies have been taken into account. These values are zero for even-even nuclides, but can be larger for odd-odd and odd-A nuclides [53].
To place the previously observed α-energies correctly into the α-decay schemes the full spectroscopy information in the mass region under interest was taken into account. The α-decay energies have been accumulated from the review works [12, 54, 55, 56] and from recent original works [57] - [74] .

A few linked α-decay chains are given in Figs. 9 -11 as an example. The nuclides whose masses have been measured directly are indicated by boxes in these figures. The energies of α-particles in keV as well as the half-lives and spin-values are shown . The choice of this illustration comes from the necessity to show that there is a big variety of decay links within the chains. Fig.9 gives an example how from directly measured mass value for ^{195}Tl (which should belong to the ground state) one can obtain the masses for other nuclides by the scheme ^{195}Tl $\rightarrow$ ^{199m}Bi $\rightarrow$ ^{199g}Bi $\rightarrow$ ^{203}At $\rightarrow$ ^{207}Fr $\rightarrow$ ^{211}Ac $\rightarrow$ ^{215}Pa. More complicated path for mass determination ensues from the α-links shown in Fig.10. Here we can start from directly measured mass value for ^{193}Bi, which is in it's ground state. One can obtain masses for all the nuclides linked by α-transitions (from ^{189}Tl to ^{201}Fr). The so called "unfavored" cases are shown in Fig.11. Here the directly measured mass values cannot be alternatively attributed to ground or isomeric states in both nuclides: ^{192}Tl and ^{196}Bi.

The weighted average Q_α-values for the nuclides of interest are given in Table 3. We used these values to determine the masses of nuclides within α-decay chains, which are marked by symbol A in Table 4.

4 Table of masses

The mass values determined in this work are presented in Table 4.

Table 2: α -Decay chains connected to the end point nuclides, which masses have been directly measured by Schottky mass-spectrometry. Directly measured masses within the chains are indicated by bold symbols

Nuclide, $(T_{1/2})$	Nuclides in the α-decay chains, $(T_{1/2})$
$^{164}\mathbf{Hf}$ $(114\ s)$	$^{168}W(53\ s)$;$^{172}Os(19\ s)$;$^{176}Pt(6.3\ s)$;$^{180}Hg(2.6\ s)$;$^{184}Pb(0.55\ s)$
$^{170}\mathbf{W}$ $(2.4\ min)$	$^{174}\mathbf{Os}(45\ s)$; $^{178}\mathbf{Pt}(21\ s)$;$^{182}Hg(11\ s)$;$^{186}Pb(4.8\ s)$;$^{190}Po(2.4\ ms)$
$^{173}\mathbf{Re}$ $(2\ min)$	$^{177}\mathbf{Ir}(30\ s)$; $^{181}\mathbf{Au}(14.5\ s)$;$^{185m}Tl(1.8\ s)$;$^{189}Bi(0.68\ s)$;$^{193}At(34\ ms)$
$^{175}\mathbf{Os}$ $(1.4\ min)$	$^{179}\mathbf{Pt}(21\ s)$;$^{183}Hg(8.8\ s)$;$^{187}Pb(15\ s)$;$^{191}Po(22\ ms)$;$^{195}Rn(\approx 6ms)$
$^{176}\mathbf{Os}$ $(3.6\ min)$	$^{180}\mathbf{Pt}(52\ s)$; $^{184}\mathbf{Hg}(30.6\ s)$; $^{188}\mathbf{Pb}(25.5\ s)$;$^{192}Po(38\ ms)$;$^{196}Rn(4.4\ ms)$
$^{177}\mathbf{Os}$ $(2.8\ min)$	$^{181}\mathbf{Pt}(51\ s)$; $^{185}\mathbf{Hg}(49\ s)$; $^{189}\mathbf{Pb}(51\ s)$;$^{193}Po(0.36\ s)$;$^{197}Rn(65\ ms)$
$^{178}\mathbf{Os}$ $(5\ min)$	$^{182}\mathbf{Pt}(2.6\ min)$; $^{186}\mathbf{Hg}(1.4\ min)$; $^{190}\mathbf{Pb}(1.2\ min)$;$^{194}Po(0.39\ s)$; $^{198}Rn(64\ ms)$;$^{202}Ra(0.7\ ms)$
$^{179}\mathbf{Os}$ $(6.3\ min)$	$^{183}\mathbf{Pt}(6.5\ min)$; $^{187}\mathbf{Hg}(2.4\ min)$; $^{191}\mathbf{Pb}(1.3\ min)$;$^{195}Po(4.6\ s)$; $^{199}Rn(0.62\ s)$;$^{203}Ra(1\ ms)$
$^{180}\mathbf{Os}$ $(22\ min)$	$^{184}\mathbf{Pt}(17\ min)$; $^{188}\mathbf{Hg}(3.2\ min)$; $^{192}\mathbf{Pb}(3.5\ min)$;$^{196}Po(5.8\ s)$; $^{200}Rn(1\ s)$;$^{204}Ra(59\ ms)$
$^{178}\mathbf{Ir}(12\ s)$	$^{182}\mathbf{Au}(15\ s)$;$^{186m}Tl(26\ s)$;$^{190}Bi(6.3\ s)$;$^{194}At(0.18\ s)$
$^{179}\mathbf{Ir}(79\ s)$	$^{183}\mathbf{Au}(45\ s)$;$^{187m}Tl(16\ s)$;$^{191}Bi(12\ s)$;$^{195}At(0.4\ s)$
$^{190}\mathbf{Hg}(20\ min)$	$^{194}\mathbf{Pb}(12\ min)$; $^{198}\mathbf{Po}(1.8\ min)$;$^{202}Rn(9.8\ s)$;$^{206}Ra(0.24\ s)$;$^{210}Th(9\ ms)$
$^{188}\mathbf{Tl}(1.2\ min)$	$^{192}\mathbf{Bi}(35\ s)$;$^{196}At(0.39\ s)$;$^{200}Fr(19\ ms)$
$^{189}\mathbf{Tl}(2.3\ min)$	$^{193}\mathbf{Bi}(67\ s)$;$^{197}At(0.39\ s)$;$^{201}Fr(69\ ms)$
$^{190}\mathbf{Tl}(2.6\ min)$	$^{194}\mathbf{Bi}(95\ s)$;$^{198}At(4.2\ s)$;$^{202}Fr(0.34\ s)$;$^{206}Ac(22\ ms)$
$^{191}\mathbf{Tl}$	$^{195}\mathbf{Bi}(3\ min)$;$^{199}At(7.2\ s)$;$^{203}Fr(0.55\ s)^{207}Ac(27\ ms)$
$^{192}\mathbf{Tl}(9.6\ min)$	$^{196}\mathbf{Bi}(5\ min)$;$^{200}At(43\ s)$;$^{204}Fr(1.5\ s)$;$^{208}Ac(95\ ms)$;$^{212}Pa(5\ ms)$
$^{193}\mathbf{Pb}(4\ min)$	$^{197}\mathbf{Po}(54\ s)$;$^{201}Rn(7\ s)$;$^{205}Ra(0.21\ s)$;$^{209}Th(4\ ms)$
$^{195}\mathbf{Pb}(15\ min)$	$^{199}\mathbf{Po}(5.5\ min)$;$^{203}Rn(45\ s)$;$^{207}Ra(1.3\ s)$;$^{211}Th(37\ ms)$
$^{196}\mathbf{Pb}(36\ min)$	$^{200}\mathbf{Po}(12\ min)$;$^{204}Rn(1.2\ min)$;$^{208}Ra(1.3\ s)$;$^{212}Th(30\ ms)$
$^{197}\mathbf{Pb}(8\ min)$	$^{201}\mathbf{Po}(15\ min)$;$^{205}Rn(2.8\ min)$;$^{209}Ra(4.6\ s)$;$^{213}Th(0.14\ s)$
$^{198}\mathbf{Pb}(2.4\ h)$	$^{202}\mathbf{Po}(45\ min)$;$^{206}Rn(5.7\ min)$;$^{210}Ra(3.7\ s)$;$^{214}Th(0.1\ s)$;$^{218}U(1.5\ ms)$
$^{197}\mathbf{Bi}(9.3\ min)$	$^{201}At(1.5\ min)$;$^{205}Fr(3.8\ s)$;$^{209}Ac(90\ ms)$;$^{213}Pa(5.3\ ms)$
$^{198}\mathbf{Bi}(10\ min)$	$^{202}At(3\ min)$;$^{206}Fr(16\ s)$;$^{210}Ac(0.35\ s)$;$^{214}Pa(17\ ms)$

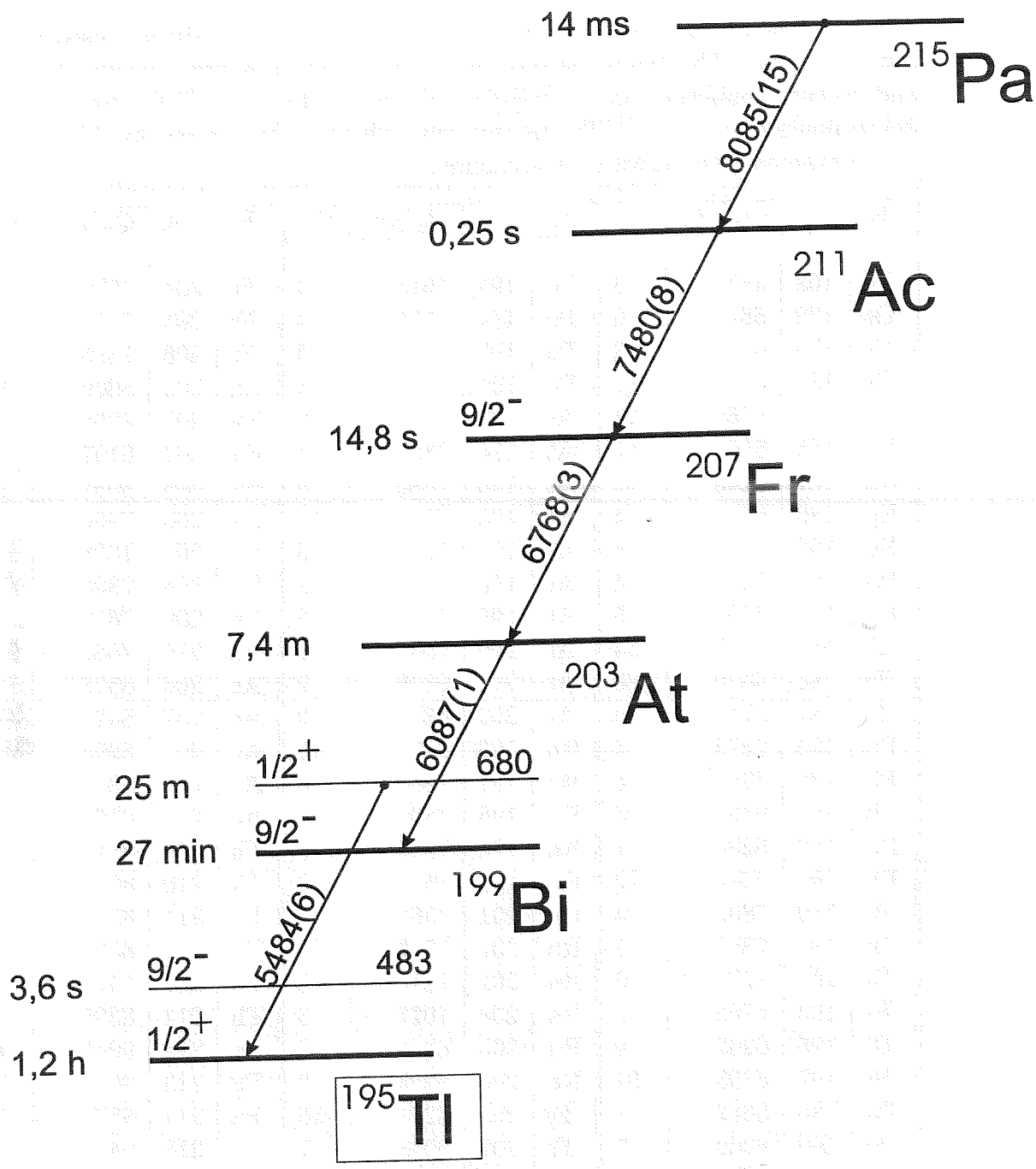

Figure 9: α-Decay chain started from ^{215}Pa. Kinetic energies of α-particles and excitation energies of nuclides are given in keV. Nuclides whose masses were measured directly by SMS are indicated by boxes.

Table 3: The averaged α-decay energies and their eror bars (in μu) used for the mass determination. The averaging has been done by using review articles [12, 54, 55, 56] and recently published works [57]-[74]. Q_α-values for ^{193,195,197}Bi were used for mass determination of ^{189,191,193}Tl, respectively, whereas the masses for bismuth nuclides were obtained from direct measurements.

El	A	$Q_\alpha(\mu u)$	Err	El	A	$Q_\alpha(\mu u)$	Err	El	A	$Q_\alpha(\mu u)$	Err
W	168	4838	13	Po	193	7615	4	Fr	204	7699	3
Os	172	5610	6	Po	194	7503	3	Fr	205	7573	3
Pt	176	6319	3	Po	195	7243	3	Fr	206	7436	5
Pt	183	5173	11	Po	196	7146	3	Ra	202	8609	66
Pt	185	4765	11	At	193	8041	6	Ra	203	8298	22
Au	185	5562	11	At	194	7881	6	Ra	204	8197	9
Au	187	5145	22	At	195	7880	5	Ra	205	8037	22
Hg	180	6718	4	At	196	7548	16	Ra	206	7960	5
Hg	182	6438	5	At	197	7624	3	Ra	207	7808	3
Hg	183	6483	4	At	198	7400	3	Ra	208	7808	5
Hg	185	6203	5	At	199	7278	3	Ra	209	7672	5
Tl	185	6107	54	At	200	7081	2	Ra	210	7682	5
Tl	186	6320	160	At	201	6949	2	Ac	206	8528	32
Tl	187	5717	13	At	202	6829	2	Ac	207	8421	27
Pb	184	7272	4	Rn	196	8177	10	Ac	208	8295	15
Pb	186	6947	6	Rn	197	7955	8	Ac	209	8302	10
Pb	187	6867	8	Rn	198	7890	4	Ac	210	8166	9
Pb	189	6284	11	Rn	199	7656	6	Th	209	8843	76
Pb	191	5944	22	Rn	200	7562	3	Th	210	8645	18
Bi	189	7802	4	Rn	201	7365	2	Th	211	8527	15
Bi	190	7367	5	Rn	202	7272	2	Th	212	8537	11
Bi	191	7279	3	Rn	203	7117	3	Th	213	8415	8
Bi	193	6765	9	Rn	204	7027	3	Th	214	8399	8
Bi	195	6262	9	Rn	205	6856	2	Pa	212	9049	60
Bi	197	5793	54	Rn	206	6853	2	Pa	213	9011	21
Po	188	8682	7	Fr	200	8271	16	Pa	214	8879	21
Po	190	8262	7	Fr	201	8068	7	U	218	9432	21
Po	191	8039	9	Fr	202	7932	6				
Po	192	7858	8	Fr	203	7812	5				

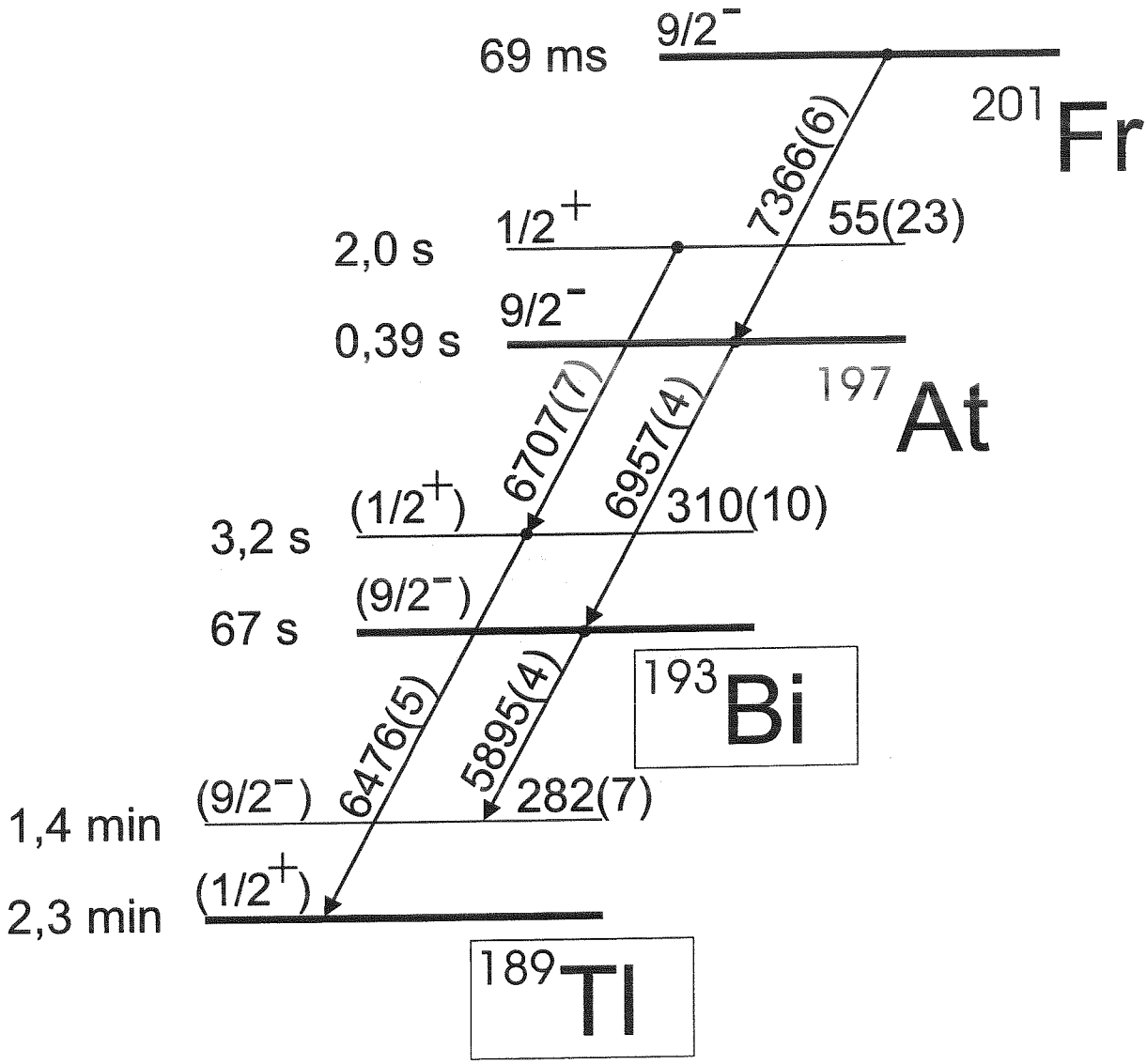

Figure 10: α-Decay chain started from ^{201}Fr. Definitions are as in Fig.9.

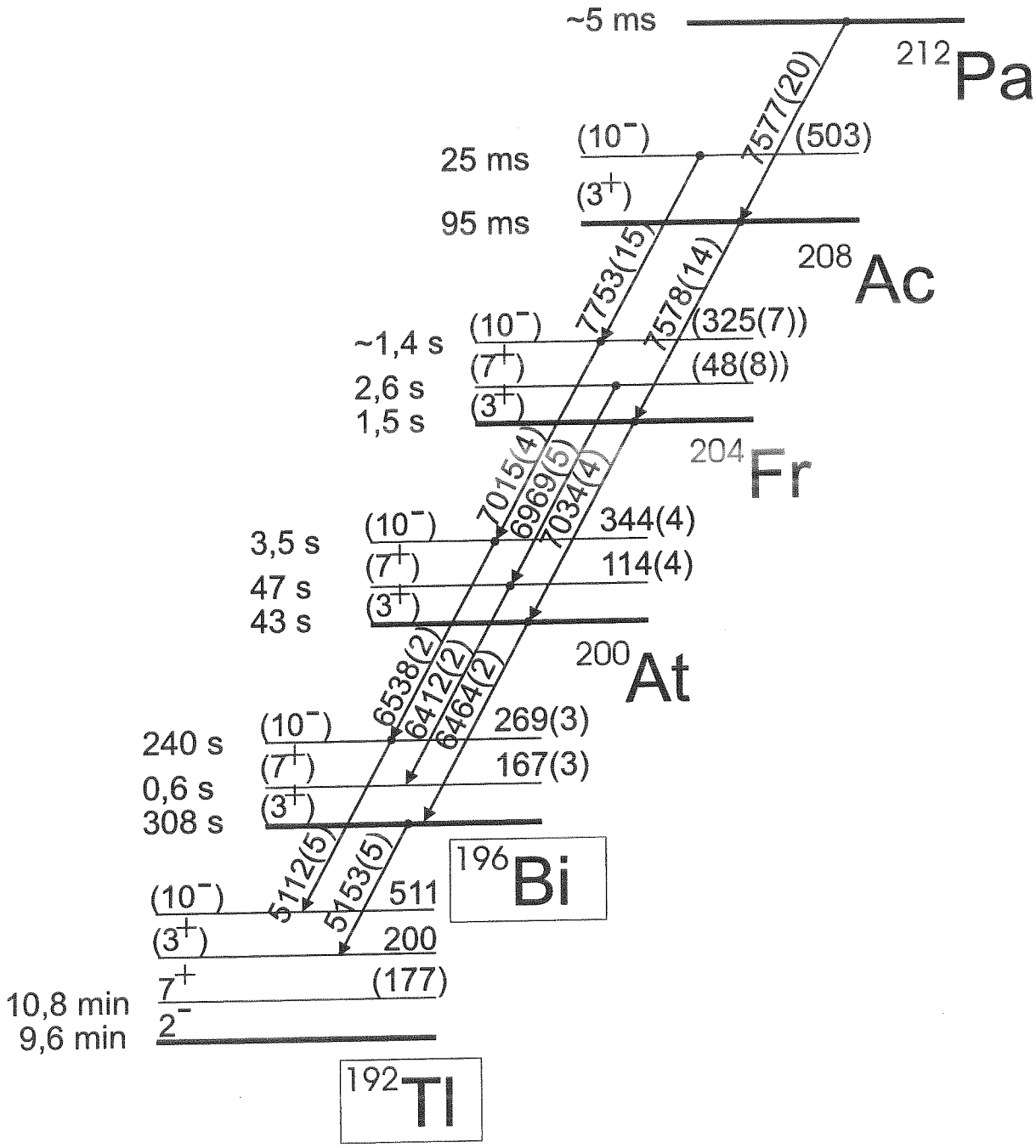

Figure 11: α-Decay chain started from ^{212}Pa. Definitions are as in Fig.9.

The mass values for 168 nuclides have been determined for the first time. In addition, for 27 nuclides whose mass values were known previously with a precision of worse than 150 keV we give the reevaluated values (labeled by index r in the Table 4).
The atomic mass values for nuclides are given in the fifth column in atomic units (u). The error bars for mass values are shown in the sixth column. These errors, rounded by the last digit, are the square root of the sum of the squared statistical and squared systematic errors. The systematical error equals to 100 μu as it was mentioned above (see subsection 3.3). The mass excess values are given with error bars in keV in the seventh and eighth columns, respectively. Table 4 contains directly measured values (label D in the last column) and the values determined by means of α-spectroscopy information (label A). To determine the mass values measured directly by SMS we used the set of reference nuclides with well known mass values [13]. These nuclides are listed in Table 5. Known [12] and updated Q_α-values (see Table 6) were used for additional links between nuclides with unknown masses, measured directly by SMS. Only nuclides without isomeric states according to [13] were used for the calibration process. Also the Q_α-values were taken only from nuclides without isomeric states The directly measured mass values presented in Table 4 have been obtained by data analysis (see section 3) using a general least square method as outlined in Ref. [75]. The evaluated mass values are correlated in a network of information which contains the repeated measurements for each isotopes in different $B\rho$ settings and ionic charge states and thus in different calibration nets within the high-resolution frequency spectra.
The mass values within the α-decay chains, marked by symbol A in Table 4, have been determined by adding the Q_α-values of Table 3 to the mass values measured by SMS in accordance with the equation (34). The values for masses and their error bars in Table 4 are rounded off values.
An inherent problem of mass measurements are unresolved isomeric states of the fragments.
The odd-odd and the odd-A isotopes of the elements from gold to polonium, have known isomeric states. In the column for comments of Table 4 we marked by asterisk those nuclides for which the isomeric states are known or those nuclides which are linked with them by α-decay chains. The energies of corresponding isomeric states are also given in keV. In principle, we cannot distinguish isomeric state if the mass difference between ground and isomeric state is less than experimental mass resolution. However, some criteria can help to estimate the admixture of an isomeric state to the frequency peak. The isomers with energies higher than 500 keV can be resolved in the spectra, whereas the states with energies of less than 100 keV can only marginally shift the frequency peaks within the quoted experimental error bars. Only isomers with half-lives of more than 10 s survive the storage and cooling time and can contribute to the frequency peak (index a in the table). The states with excitation energies in the range of 100 to 500 keV can change the position of the ground state frequency peak in the spectrum. The values of the isomeric states energies presented in the column 9 can be considered as upper limit for an additional systematic uncertainty of the mass value.
An estimation of the production yields ratios for ground and isomeric states in projectile fragmentation has been performed in Ref. [76]. Within the abrasion-ablation scheme the authors have developed a model to predict the ratio for population of ground to isomeric states as a function of the angular momentum. This model assummes a two step production mechanism of final nuclides via the prefragmentation (abrasion) pro-

Table 4: Table of masses determined for the first time.
The marks mean as follows:
^{r} - nuclides which masses were known with error bars $\geq$ 150 keV,
* - marks unfavored cases followed by the excitation energies of the corresponding isomeric states in keV,
$^{@}$ - the masses of nuclides have been obtained from directly measured masses for the bismuth isotopes and their α-decay energies,
** - tentative assignment for α-decay chain,
^{a} - the isomeric states have half-lives less than 10 s,
^{g} - the mass value belongs preferably to ground state (see text),
^{i} - the mass value belongs preferably to the isomeric state (see text)

El.	Z	N	A	Exp. mass (u)	Err (μu)	Mass exc. (keV)	Err (keV)	Comm.	
La	57	76	133	132.908200	120	-85510	110	r	D
Ce	58	76	134	133.908810	130	-84940	120	r	D
Nd	60	75	135	134.918200	130	-76200	120	*65	D
Nd	60	78	138	137.911940	130	-82030	120		D
Pm	61	77	138	137.919780	140	-74720	130	*≈80	D
Ho	67	89	156	155.929970	110	-65230	100	*52,a	D
Er	68	90	158	157.929780	110	-65410	100		D
Tm	69	89	158	157.936920	110	-58760	100	*	D
Tm	69	91	160	159.935270	120	-60300	110	*≈70,r	D
Yb	70	90	160	159.937560	120	-58160	110		D
Yb	70	91	161	160.937880	110	-57860	100		D
Yb	70	92	162	161.935790	110	-59810	100		D
Yb	70	94	164	163.934310	100	-61190	90		D
Lu	71	91	162	161.943390	140	-52730	130	*≈ 120	D
Lu	71	92	163	162.941270	110	-54710	100	r	D
Lu	71	93	164	163.941250	110	-54730	100		D
Lu	71	95	166	165.939870	110	-56010	100		D
Hf	72	92	164	163.944380	110	-51810	100		D
Hf	72	93	165	164.944640	140	-51570	130		D
Hf	72	94	166	165.942140	110	-53900	100		D
Hf	72	95	167	166.942510	110	-53550	100		D
Hf	72	96	168	167.940440	100	-55480	90		D
Hf	72	98	170	169.939600	100	-56260	90		D
Hf	72	99	171	170.940440	100	-55480	90	*≈50	D
Ta	73	94	167	166.948130	120	-48320	110		D
Ta	73	95	168	167.947980	110	-48460	100		D
Ta	73	96	169	168.946040	110	-50260	100		D
Ta	73	97	170	169.946190	100	-50120	90		D

El.	Z	N	A	Exp. mass (u)	Err (μu)	Mass exc. (keV)	Err (keV)	Comm.	
Ta	73	98	171	170.944450	100	-51740	90		D
Ta	73	100	173	172.943730	100	-52420	90		D
Ta	73	102	175	174.943650	120	-52490	110		D
W	74	94	168	167.951820	110	-44880	100		A
W	74	96	170	169.949290	110	-47240	100		D
W	74	97	171	170.949350	110	-47180	100		D
W	74	98	172	171.947230	110	-49150	100		D
W	74	99	173	172.947660	100	-48750	90		D
W	74	100	174	173.946060	100	-50240	90		D
W	74	101	175	174.946710	100	-49640	90		D
W	74	102	176	175.945580	100	-50690	90		D
W	74	103	177	176.946580	110	-49760	100		D
Re	75	97	172	171.955300	220	-41640	200	*$\leq$200,g	D
Re	75	98	173	172.953090	110	-43700	100		D
Re	75	99	174	173.953070	100	-43720	90		D
Re	75	100	175	174.951370	100	-45300	90		D
Re	75	101	176	175.951620	110	-45070	100		D
Re	75	102	177	176.950380	100	-46220	90		D
Re	75	103	178	177.951200	110	-45460	100	r	D
Os	76	96	172	171.960030	110	-37230	100		A
Os	76	98	174	173.957120	110	-39940	100		D
Os	76	99	175	174.956880	110	-40170	100		D
Os	76	100	176	175.954850	110	-42060	100		D
Os	76	101	177	176.954980	100	-41940	90		D
Os	76	102	178	177.953210	100	-43580	90	r	D
Os	76	103	179	178.953780	100	-43050	90		D
Os	76	104	180	179.952330	100	-44400	90		D
Os	76	105	181	180.953350	100	-43450	90	*49,r	D
Ir	77	100	177	176.961190	110	-36150	100		D
Ir	77	101	178	177.961050	110	-36280	100		D
Ir	77	102	179	178.959090	100	-38110	90		D
Ir	77	103	180	179.959200	100	-38000	90		D
Ir	77	104	181	180.957670	100	-39430	90	r	D
Ir	77	106	183	182.956840	100	-40200	90		D
Ir	77	107	184	183.957540	110	-39550	100	r	D
Ir	77	108	185	184.956660	110	-40370	100		D

El.	Z	N	A	Exp. mass (u)	Err (μu)	Mass exc. (keV)	Err (keV)	Comm.	
Pt	78	98	176	175.968950	110	-28920	100		A
Pt	78	100	178	177.965700	110	-31950	100		D
Pt	78	101	179	178.965290	110	-32330	100		D
Pt	78	102	180	179.963100	110	-34370	100		D
Pt	78	103	181	180.963120	100	-34350	90		D
Pt	78	104	182	181.961130	100	-36210	90	r	D
Pt	78	105	183	182.961560	100	-35810	90		A
Pt	78	106	184	183.959880	100	-37370	90		D
Pt	78	107	185	184.960720	100	-36590	90	r	A
Pt	78	109	187	186.960500	110	-36790	100		D
Au	79	102	181	180.969970	110	-27970	100		D
Au	79	103	182	181.969580	110	-28340	100		D
Au	79	104	183	182.967560	100	-30220	90		D
Au	79	105	184	183.967490	100	-30280	90		D
Au	79	106	185	184.965840	100	-31820	90	r	A
Au	79	108	187	186.964590	100	-32980	90		A
Au	79	109	188	187.965250	100	-32370	90		D
Au	79	110	189	188.964050	110	-33490	100	*247,i	D
Hg	80	100	180	179.978270	120	-20240	110		A
Hg	80	102	182	181.974740	110	-23530	100		A
Hg	80	103	183	182.974380	110	-23860	100		A
Hg	80	104	184	183.971770	110	-26300	100		D
Hg	80	105	185	184.971930	100	-26150	90		A
Hg	80	106	186	185.969340	100	-28560	90	r	D
Hg	80	107	187	186.969840	100	-28090	90	*≈100	D
Hg	80	108	188	187.967540	100	-30240	90		D
Hg	80	109	189	188.968260	100	-29570	90	*≈120	D
Hg	80	110	190	189.966330	100	-31360	90		D
Hg	80	112	192	191.965560	100	-32080	90		D
Tl	81	104	185	184.978680	120	-19860	110		A
Tl	81	105	186	185.978500	190	-20030	180		A
Tl	81	106	187	186.975880	100	-22470	90		A
Tl	81	107	188	187.976190	110	-22180	100	*≈100	D
Tl	81	108	189	188.973650	110	-24540	100	@	A
Tl	81	109	190	189.973950	100	-24270	90	*≈170	D
Tl	81	110	191	190.971820	100	-26250	90	@	A

El.	Z	N	A	Exp. mass (u)	Err (μu)	Mass exc. (keV)	Err (keV)	Comm.	
Tl	81	111	192	191.972270	100	-25830	90	*≈160	D
Tl	81	112	193	192.970510	100	-27470	90	@	A
Tl	81	113	194	193.971340	110	-26700	100	*≈300	D
Tl	81	114	195	194.969940	100	-28000	90	*480,a	D
Pb	82	102	184	183.988150	120	-11040	110		A
Pb	82	104	186	185.984290	110	-14630	100		A
Pb	82	105	187	186.983850	110	-15040	100		A
Pb	82	106	188	187.980930	110	-17760	100		D
Pb	82	107	189	188.980810	100	-17880	90		A
Pb	82	108	190	189.978060	100	-20440	90	r	D
Pb	82	109	191	190.978230	110	-20280	100	*≈90	D
Pb	82	110	192	191.975750	100	-22590	90		D
Pb	82	111	193	192.976210	100	-22160	90	*≈130	D
Pb	82	112	194	193.974020	100	-24200	90		D
Pb	82	113	195	194.974690	100	-23580	90	*203	D
Pb	82	114	196	195.972800	100	-25340	90		D
Pb	82	115	197	196.973480	110	-24700	100	*319	D
Pb	82	116	198	197.972010	100	-26070	90		D
Bi	83	106	189	188.989080	120	-10170	110		A
Bi	83	107	190	189.988470	190	-10740	180		A
Bi	83	108	191	190.985760	100	-13260	90		A
Bi	83	109	192	191.985290	120	-13700	110	*≈210	D
Bi	83	110	193	192.983020	110	-15820	100	*308,a	D
Bi	83	111	194	193.982960	100	-15870	90	*≈100	D
Bi	83	112	195	194.980680	100	-18000	90		D
Bi	83	113	196	195.980840	100	-17850	90	*270	D
Bi	83	114	197	196.978910	100	-19650	90	r	D
Bi	83	115	198	197.979230	100	-19350	90	*≈150,r	D
Po	84	104	188	187.999430	120	-530	110		A
Po	84	106	190	189.995160	110	-4510	100		A
Po	84	107	191	190.994490	110	-5130	100		A
Po	84	108	192	191.991390	110	-8020	100		A
Po	84	109	193	192.991030	100	-8360	90		A
Po	84	110	194	193.988160	100	-11030	90	r	A
Po	84	111	195	194.988080	110	-11100	100	*≈90(^{191}Pb)	A
Po	84	112	196	195.985470	100	-13530	90		A
Po	84	113	197	196.985690	120	-13330	110	*≈230	D
Po	84	114	198	197.983400	100	-15460	90		D

El.	Z	N	A	Exp. mass (u)	Err (μu)	Mass exc. (keV)	Err (keV)	Comm.	
Po	84	115	199	198.983920	100	-14980	90	*312	D
Po	84	116	200	199.981830	100	-16930	90		D
Po	84	117	201	200.982470	100	-16330	90	*424	D
Po	84	118	202	201.980730	100	-17950	90		D
At	85	108	193	192.999730	120	-250	110		A
At	85	109	194	193.998960	190	-970	180		A
At	85	110	195	194.996240	100	-3500	90		A
At	85	111	196	195.995440	120	-4250	110	**	A
At	85	112	197	196.993240	110	-6300	100		A
At	85	113	198	197.992970	100	-6550	90	*$\approx$100(^{194}Bi)	A
At	85	114	199	198.990560	100	-8790	90		A
At	85	115	200	199.990520	100	-8830	90	*270(^{196}Bi)	A
At	85	116	201	200.988460	100	-10750	90	r	A
At	85	117	202	201.988660	100	-10560	90	*$\approx$150(^{198}Bi),r	A
Rn	86	110	196	196.002210	110	2060	100		A
Rn	86	111	197	197.001590	100	1480	90		A
Rn	86	112	198	197.998660	100	-1250	90	r	A
Rn	86	113	199	198.998340	110	-1550	100	*$\approx$90(^{191}Pb)	A
Rn	86	114	200	199.995630	100	-4070	90		A
Rn	86	115	201	200.995650	120	-4050	110	*$\approx$230(^{197}Po)	A
Rn	86	116	202	201.993270	100	-6270	90		A
Rn	86	117	203	202.993640	100	-5920	90	*312(^{199}Po)	A
Rn	86	118	204	203.991460	100	-7950	90		A
Rn	86	119	205	204.991920	100	-7530	90	*424(^{201}Po)	A
Rn	86	120	206	205.990180	100	-9150	90		A
Fr	87	113	200	200.006310	120	5880	110	**	A
Fr	87	114	201	201.003910	110	3640	100		A
Fr	87	115	202	202.003500	100	3260	90	*$\approx$100(^{194}Bi)	A
Fr	87	116	203	203.000980	100	910	90		A
Fr	87	117	204	204.000820	100	760	90	*270(^{196}Bi)	A
Fr	87	118	205	204.998640	100	-1270	90	r	A
Fr	87	119	206	205.998700	100	-1210	90	*$\approx$150(^{198}Bi),r	A
Ra	88	114	202	202.009870	120	9190	110		A
Ra	88	115	203	203.009240	110	8610	100	*$\approx$90(^{191}Pb)	A
Ra	88	116	204	204.006430	100	5990	90		A
Ra	88	117	205	205.006290	120	5860	110	*$\approx$230(^{197}Po)	A
Ra	88	118	206	206.003830	100	3570	90		A

El.	Z	N	A	Exp. mass (u)	Err (μu)	Mass exc. (keV)	Err (keV)	Comm.	
Ra	88	119	207	207.004060	100	3780	90	*312(^{199}Po)	A
Ra	88	120	208	208.001870	100	1740	90		A
Ra	88	121	209	209.002200	100	2050	90	*424(^{201}Po)	A
Ra	88	122	210	210.000470	100	440	90		A
Ac	89	117	206	206.014630	110	13630	100	*$\approx$100(^{194}Bi)	A
Ac	89	118	207	207.012000	110	11180	100		A
Ac	89	119	208	208.011720	100	10920	90	*270(^{196}Bi)	A
Ac	89	120	209	209.009540	100	8890	90	r	A
Ac	89	121	210	210.009470	100	8820	90	*$\approx$150(^{198}Bi),r	A
Th	90	119	209	209.017740	150	16520	140	*$\approx$230(^{197}Po)	A
Th	90	120	210	210.015080	100	14050	90		A
Th	90	121	211	211.015190	110	14150	100	*312((^{199}Po)	A
Th	90	122	212	212.013010	100	12120	90		A
Th	90	123	213	213.013220	100	12310	90	*424(^{201}Po)	A
Th	90	124	214	214.011470	100	10680	90		A
Pa	91	121	212	212.023370	120	21770	110	*270(^{196}Bi)	A
Pa	91	122	213	213.021160	110	19710	100	r	A
Pa	91	123	214	214.020950	110	19510	100	*$\approx$150(^{198}Bi),r	A
U	92	126	218	218.023510	110	21900	100		A

cess with subsequent evaporation of the nucleons from prefragments (ablation).

We have estimated the isomeric ratios for the reaction ^{209}Bi projectiles in beryllium. These ratios have been obtained by means of the equation (see ref. [76]):

$$\frac{Y(J_{gs})}{Y(J_{is})} = \frac{2J_{gs}+1}{2J_{is}+1} * exp(-\frac{J_{gs}(J_{gs}+1) - J_{is}(J_{is}+1)}{2\sigma_f^2}), \tag{35}$$

where the spin cut-off parameter σ_f^2 is given by

$$\sigma_f^2 = 0.018 A_p^{2/3} \frac{(A_p - A_f)(2A_p + A_f)}{A_p - 1}, \tag{36}$$

if one assume that the number of evaporated nucleons in the ablation step is proportional to the mass loss induced by the abrasion stage with a factor of proportionality equal to 2 [76]. The A_p and A_f in the formula stands for the mass numbers for projectile and the fragment, respectively. The results are presented in Table 7 .
One can see from this table that in fragmentation reaction with bismuth projectiles the ground state production is predominantly populated for the nuclides ^{172}Re, ^{183}Os, ^{185}Pt and ^{195}Bi , whereas the isomeric states are more probable to be produced for nuclides ^{189}Au, ^{187}Tl, ^{189}Tl, ^{191}Tl and ^{193}Tl. For some of mentioned nuclides this preferable identification is indicated in Table 4 by index g (ground state) and i (isomeric state).

Table 5: Table of reference nuclei used for determining the masses shown in Table 4. Nuclides which were compared to [12] to determine the systematic error are marked with an ^{s}.

Z	A	Z	A	Z	A	Z	A	Z	A	Z	A
53	125	64	150	68	160^s	72	176	78	189	83	202^s
54	126	64	151	68	161	73	174^s	78	190	83	203
58	136^s	64	152	68	162	73	176^s	78	191	83	204
60	140	65	153	68	163	73	181	78	192	83	205
61	141	66	151	69	159^s	74	178^s	79	186^s	83	206
61	143	66	152	69	161^s	74	180	79	190	83	207
61	144	66	153	69	163	74	181	79	192	83	208
61	145	66	154	70	159^s	75	179^s	79	194	83	209
62	140	66	155	70	163^s	75	180^s	79	199	84	204
62	142	66	156	70	165	75	181	80	194	84	205^s
62	145	66	157	70	166	75	189	80	196	84	206
62	146	66	158	70	167	76	182	80	198	84	208
63	145	67	155	70	168	76	184	81	197^s	85	203^s
63	146	67	157^s	70	173	76	186	81	199^s	85	204^s
63	147	68	154	71	167^s	77	182^s	81	200	85	205^s
63	148	68	155^s	71	170	77	188	81	201		
64	147	68	156^s	72	169^s	77	189	81	202		
64	148	68	157^s	72	172^s	78	186^s	82	200		
64	149	68	159	72	174	78	188	82	202		

Table 6: Table of Q_α values and their errors (in keV) used for calibration for the determination of the masses shown in Table 4. Except for ^{177}Ir,^{180}Pt, and ^{181}Pt [55], the listed values were taken from [12].

Z	A	Q_α	ΔQ_α	Z	A	Q_α	ΔQ_α
76	174	4872	10	80	184	5658	15
77	177	5127	10	80	186	5206	15
78	178	5570	3	80	188	4711	20
78	179	5415	10	82	188	6112	3
78	180	5256	10	82	190	5701	4
78	181	5150	5	82	192	5222	5
78	182	4952	5	82	194	4738	20
78	184	4602	10	84	198	6309	2
79	181	5749	3	84	200	5982	2
79	182	5527	5	84	202	5700	2
79	183	5465	3				

Table 7: Predicted ratios for ground to isomeric states yields. Index "a" marks the values taken from [13], J represents the spin value and Y - production yield.

Element	A	Energy of I.S.(keV)	$J_{g.s.}$	$J_{i.s.}$	$Y_{g.s.}/Y_{i.s.}$	Comments
Tm	158	-	2	5	0.52	$(i.s.+g.s.)$
Lu	162	120(200)[a]	1	4	0.37	$(i.s.+g.s.)$
Re	172	0(200)[a]	5	2	1.83	$(g.s.)$
Os	183	170.7(1)	9/2	1/2	3.87	$g.s.$
Pt	185	103.4(2)	9/2	1/2	3.80	$g.s.$
Au	185	-	5/2	11/2	0.68	$(i.s.+g.s.)$
Au	189	247.2(2)	1/2	11/2	0.27	$i.s.$
Hg	187	100(70)[a]	3/2	13/2	0.50	$i.s.+g.s.$
Hg	189	120(80)[a]	3/2	13/2	0.53	$i.s.+g.s.$
Tl	186	0(150)[a]	2	7	0.61	$i.s.+g.s.$
Tl	187	335(7)	1/2	9/2	0.26	$i.s.$
Tl	189	282(7)	1/2	9/2	0.28	$i.s.$
Tl	190	60(60)	2	7	0.68	$i.s.+g.s.$
Tl	191	297(7)	1/2	9/2	0.29	$i.s.$
Tl	192	160(50)[a]	2	7	0.74	$i.s.+g.s.$
Tl	193	370(5)	1/2	9/2	0.30	$i.s.$
Tl	194	300(200)[a]	2	7	0.82	$i.s.+g.s.$
Tl	196	394(1)	2	7	0.94	$i.s.+g.s.$
Pb	189	70(70)	3/2	13/2	0.53	$i.s.+g.s.$
Pb	191	138(10)	3/2	13/2	0.56	$i.s.+g.s.$
Pb	193	100((50)	3/2	13/2	0.61	$i.s.+g.s.$
Pb	195	201(4)	3/2	13/2	0.68	$i.s.+g.s.$
Pb	197	319.3(1)	3/2	13/2	0.79	$i.s.+g.s.$
Bi	192	100(100)	3	10	1.60	$g.s.+i.s.$
Bi	194	150(60)	3	7	0.74	$i.s.+g.s.$
Bi	195	399(6)	9/2	1/2	3.14	$g.s.$
Bi	196	269(3)	3	10	2.56	$g.s.+i.s.$
Bi	197	510(50)[a]	9/2	1/2	2.91	$g.s.+i.s.$
Bi	198	100(65)	3	7	1.37	$g.s.+i.s.$

For some of our directly measured nuclides which may have an unresolved isomeric contribution, α-spectroscopy delivers the possibility to obtain the ground state mass value in an unambigious way. These ground state masses have been determined by adding known α-decay energies for their directly measured daughter nuclide or by subtracting them from the directly measured mother nuclide.

5 Masses of isomeric states with unknown excitation energies

For the nuclides very far off the β-stability line the isomeric states have been mostly identified by their α-decay. The observation of the ground state α-decay was very often accompanied by identification of the α-transition from the isomeric state too. Thus, the α-decay chains appeared within the isomeric states in parallel to the ground states chains (see,e.g., Fig.11). The excitation energies of these isomeric states were unknown so far.
For some of the nuclides at the ends of the α-chains the isomeric state energies are precisely known from γ-spectroscopy. Then the possibility to determine their mass values and hence the masses for the members of corresponding α-chains depends on whether the mass values for the ground states of the end nuclides are known.
The directly measured mass values by SMS again open such type possibility. However, using these data we have to be sure that they belong entirely to the ground (or isomeric) states. Another problem is a knowledge of the α-decay schemes within the isomeric chains which connect the odd-A or odd-odd nuclides. During the last few years the recoil $\alpha - \alpha$-correlation method was successfully used for the identification of new nuclides and of the genetic relations between various α-transitions (see ref. [58] and references therein). Though the uncertainties in the α-decay schemes still can exist, the precision of the Q_α-value determination is expected to be much better than the error bars for directly measured masses which typically are on the level of $\sim$ 100 keV.

There are nuclides on the ends of chains for which the energies of isomeric states are unknown though the α -chains are completely linked. We tried to determine these energies by investigating systematical trends in behavior of known similar levels in neighbor nuclides. Therefore such type predictions are expected to be less precise but for some physical goals discussed in this article they could be useful.
Isomeric states with unknown energies for odd-odd nuclides (with $105 \leq N \leq 119$) are shown in Fig. 12 where the energies for other known isotopes of elements are accumulated as well.
Due to the linking various isomeric states by α-transitions we can predict the unknown energies of isomeric states (marked by symbols s,t,x,y,z in Fig. 12) by using a system of unequalities:

$$\left\{\begin{array}{lll} 0 \leq x \leq 180(Tl) & 0 \leq y \leq 167(Bi) & y - 95 \geq z(At) \\ 301 + x \leq 511(Tl) & y - 95 \leq 104(At) & 297 + y \leq 587 + z(Fr) \\ 94 + x \leq 269(Bi) & 335 \leq 297 + y(At) & \\ 196 + x \leq 335(At) & 316 \leq 436 + y(Fr) & \\ 195 + x \leq 316(Fr) & 269 \leq 248 + y \leq 428(Bi) & \end{array}\right\}$$

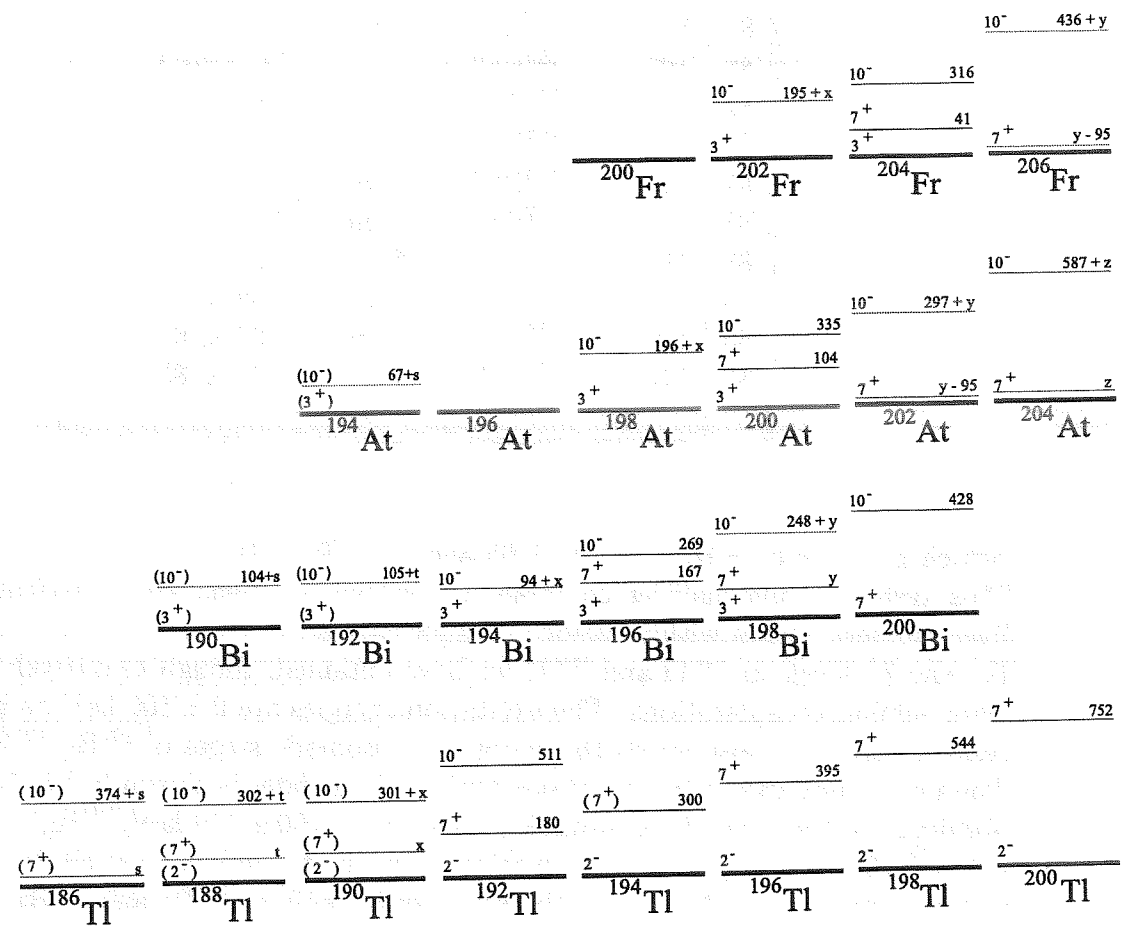

Figure 12: Systematics of the long-lived isomeric states for odd-odd nuclides with neutron numbers in the range $105 \leq N \leq 119$. The unknown level energies for ^{186}Tl, ^{188}Tl,^{190}Tl,^{198}Bi and ^{204}At are marked as s, t, x, y, z. Unknown energies for other isomeric states are expressed via these values due to the known α-decay energies. Unknown values have been obtained by using the net-method (see text). All values are given in keV.

Table 8: Energies of the isomeric states at the ends of α-decay chains which values have been taken from electron and γ-spectroscopy [13, 55] or derived in this work from systematics (marked by symbol (*)).

Z	N	Isom.Nucl.	Half-life	Energy in keV
81	107	$^{188}Tl^{m}$	$\approx$ 70 s	0 $\pm$ 100 (*)
81	109	$^{190}Tl^{m}$	3.7 min	60 $\pm$ 60 (*)
82	107	$^{189}Pb^{m}$	-	70 $\pm$ 70 (*)
82	109	$^{191}Pb^{m}$	2.2 min	138 $\pm$ 10
82	111	$^{193}Pb^{m}$	5.8 min	100 $\pm$ 50 (*)
82	113	$^{195}Pb^{m}$	15 min	201 $\pm$ 4
82	115	$^{197}Pb^{m}$	43 min	319.3 $\pm$ 0.1
83	113	$^{196}Bi^{m_1}$	0.6 s	167 $\pm$ 3
83	113	$^{196}Bi^{m_2}$	240 s	269 $\pm$ 3
83	115	$^{198}Bi^{m_1}$	11.5 min	100 $\pm$ 65 (*)
83	115	$^{198}Bi^{m_2}$	7.7 s	348 $\pm$ 65 (*)

which give $x = 60 \pm 60$; $y = 100 \pm 65$ and $z = -90 \pm 165$.
This system of unequalities combines the systematic behavior of excitations of long-lived isomeric states within various isotopic chains.
For the 7^+ levels in ^{188}Tl and ^{186}Tl we have obtained, though tentatively, the energies using similar considerations. The excitation energies are 0 ± 100 keV and 0 ± 150 keV, respectively. This also yields the energies for isomeric states of ^{192}Bi, ^{190}Bi and ^{194}At.
The net of long-lived isomeric states for odd-A nuclides is shown in Fig.13. The values obtained for the energies of isomeric states are x=100 ± 100 keV(^{183}Hg) and y=70 ± 70 keV (^{189}Pb), which give an information about so far unknown excitation energies for isomeric states of ^{187}Pb and for the very exotic nuclides ^{193}Po and ^{197}Rn.

The energies and other spectroscopic information for the isomeric states at the ends of the isomeric α-decay chains are given in Table 8.
The mass values for isomeric states which excitation energies were unknown so far are presented in Table 9. These values have been determined by means of Q_α-values assumed from [13, 55, 56].

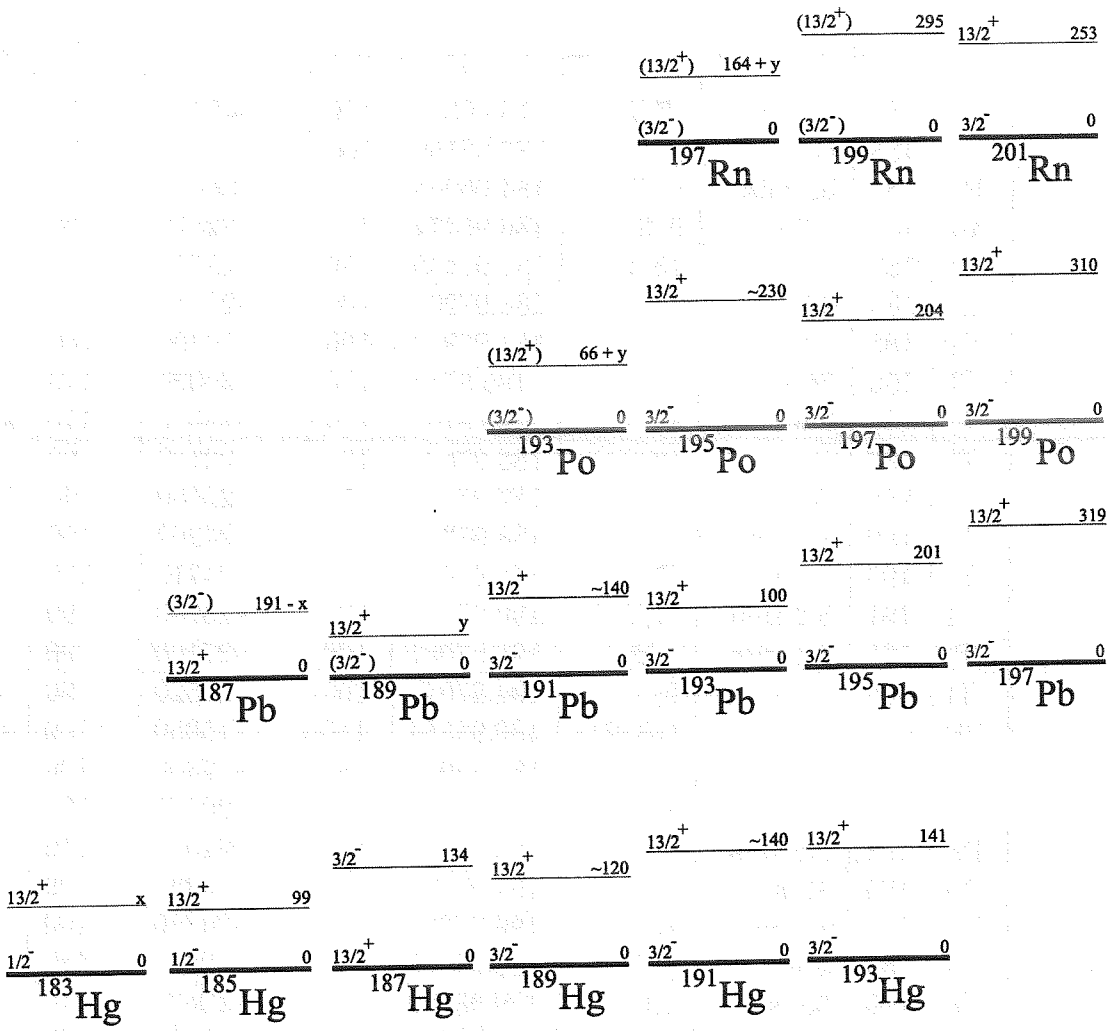

Figure 13: Systematics of the long-lived isomeric states for odd-A nuclides with neutron numbers in the range $103 \leq N \leq 115$. The unknown isomeric levels expressed via x and y have been obtained by systems of unequalities (see text). All energies are given in keV.

Table 9: The masses for isomeric states of exotic nuclides whose excitation energies are unknown. Index ^{r} represents remeasured mass value, ^{s} means that the energy of isomeric state of the "end point" nuclide has been determined from systematics, * shows "unfavored" case (see text) and, ** - tentative assumption.

El	A	Half-life	Spin	Mass (u)	Err. (u)	Mass exc. (keV)	Err. (keV)	
Os	181	2.7 min	$(7/2)^-$	180.9534	100	-43410	90	r
Pt	183	43 s	$(7/2)^-$	182.96159	100	-35770	90	
Pt	185	33 min	$(1/2^-)$	184.96083	100	-36490	90	r
Au	187	2.3 s	$9/2^-$	186.96472	100	-32870	100	
Hg	183	-	$13/2^+$	182.97449	150	-23770	140	s
Hg	185	22 s	$13/2^+$	184.97203	100	-26050	90	
Tl	185	1.8s	$9/2^-$	184.97917	150	-19400	140	**
Tl	186	26 s	7^+	185.9785	110	-20020	110	s
Tl	186	2.9 s	10^-	185.9789	110	-19650	110	s
Tl	187	16 s	$(9/2^-)$	186.97624	100	-22130	90	
Tl	188	70 s	7^+	187.97619	150	-22180	140	*,s
Tl	189	1.4 min	$9/2^{(-)}$	188.97395	110	-24260	100	
Tl	190	3.7 min	(7^+)	189.97401	120	-24210	110	s
Tl	191	5.2 min	$(1/2^+)$	190.97213	100	-25960	90	
Tl	193	2.1 min	$1/2^{(+)}$	192.97091	100	-27100	90	
Tl	195	3.6 s	$9/2^-$	194.97046	100	-27520	90	
Pb	187	15 s	$(13/2^+)$	186.98384	110	-15050	100	s
Pb	189	-	$13/2^+$	188.98089	130	-17800	120	s
Pb	191	2.2 min	$13/2^{(+)}$	190.97824	110	-20270	100	
Pb	193	5.8 min	$13/2^{(+)}$	192.97632	110	-22060	110	*
Pb	195	15 min	$13/2^+$	194.97491	100	-23380	90	*
Pb	197	43 min	$13/2^+$	196.97382	110	-24380	100	*
Bi	189	5 ms	$(1/2^+)$	188.98928	150	-9980	140	**
Bi	190	5.9 s	(10^-)	189.98859	110	-10630	110	s
Bi	191	0.15 s	$(1/2^+)$	190.98602	100	-13020	90	
Bi	192	40 s	(10^-)	191.98575	150	-13270	140	*,s
Bi	193	3.2 s	$(1/2^+)$	192.98335	110	-15510	100	
Bi	194	115 s	(10^-)	193.98307	120	-15770	110	s
Bi	195	87s	$(1/2^+)$	194.98111	100	-17600	90	
Bi	196	0.6 s	(7^+)	195.98102	100	-17680	90	*
Bi	196	240 s	(10^-)	195.98113	100	-17580	90	*
Bi	197	5.2 min	$(1/2^+)$	196.97945	100	-19150	90	
Bi	198	11.5 min	(7^+)	197.97934	120	-19250	110	*,s
Bi	198	7.7 s	(10^-)	197.9796	120	-19000	110	*,s
Bi	199	25 min	$(1/2^+)$	198.97855	100	-19980	90	
Po	191	22 ms	$3/2^-$	190.99449	150	-5140	140	s

El	A	Half-life	Spin	Mass (u)	Err. μ(u)	Mass exc. (keV)	Err. (keV)	
Po	193	0.26 s	$(13/2^+)$	192.99119	130	-8220	120	s
Po	195	1.9 s	$(13/2^+)$	194.98818	110	-11010	100	
Po	197	26 s	$(13/2^+)$	196.98592	110	-13120	110	*
Po	199	4.2 min	$13/2^+$	198.98415	100	-14770	90	*
Po	201	8.9 min	$13/2^+$	200.98276	110	-16060	100	*
At	193	24 ms	$(1/2^+)$	192.99984	150	-150	140	**
At	194	0.2 s	10^-	193.99903	250	-900	230	s
At	197	3.7 s	$(1/2^+)$	196.99331	110	-6240	100	
At	198	1.0 s	(10^-)	197.99318	120	-6350	110	s
At	200	47 s	(7^+)	199.99065	100	-8710	90	*
At	200	3.5 s	(10^-)	199.99089	100	-8480	90	*
At	202	182 s	(7^+)	201.98866	120	-10560	110	*,s
At	202	0.46 s	(10^-)	201.98908	120	-10170	110	*,s
Rn	197	19 ms	$13/2^+$	197.00185	130	1720	120	s
Rn	199	0.32 s	$(13/2^+)$	198.99852	110	-1380	100	
Rn	201	3.8 s	$(13/2^+)$	200.99593	130	-3790	120	*
Rn	203	28 s	$13/2^{(+)}$	202.99403	100	-5560	90	*
Fr	202	0.34 s	(10^-)	202.00371	120	3470	110	s
Fr	204	2.6 s	(7^+)	204.00088	100	820	90	*
Fr	204	1.4 s	(10^-)	204.00118	100	1100	90	*
Fr	206	16 s	(7^+)	205.9987	120	-1210	110	*,s
Fr	206	0.7s	(10^-)	205.99927	120	-680	110	*,s
Ra	203	33 ms	$(13/2^+)$	203.00946	110	8810	100	
Ra	205	0.17 s	$(13/2^+)$	205.0066	130	6150	120	*
Ra	207	55 ms	$(13/2^+)$	207.00465	100	4330	90	*
Ac	206	33 ms	(10^-)	206.01480	120	13790	110	s
Ac	208	25 ms	(10^-)	208.01227	100	11430	100	*

6 Discussion

Table 4 contains all nuclides for which the mass values have been measured for the first time or have been known with poor accuracy previously. In addition, also mass values for other nuclei are listed which were measured by other methods before but differ drastically from the systematic values given by Audi and Wapstra in Ref. [12]. Evidently, we did not use those experimental data as reference values in our data analysis and can therefore contribute to decide if the recommended values in Ref. [12] or the published experimental data are more reliable. This comparison is shown in Fig. 14, where the differences are presented between our values and the other experimental and recommended values of Ref. [12]. The result is that our data agree well with the Audi-

Wapstra recommendation but strongly disagree with the previous experimental data.

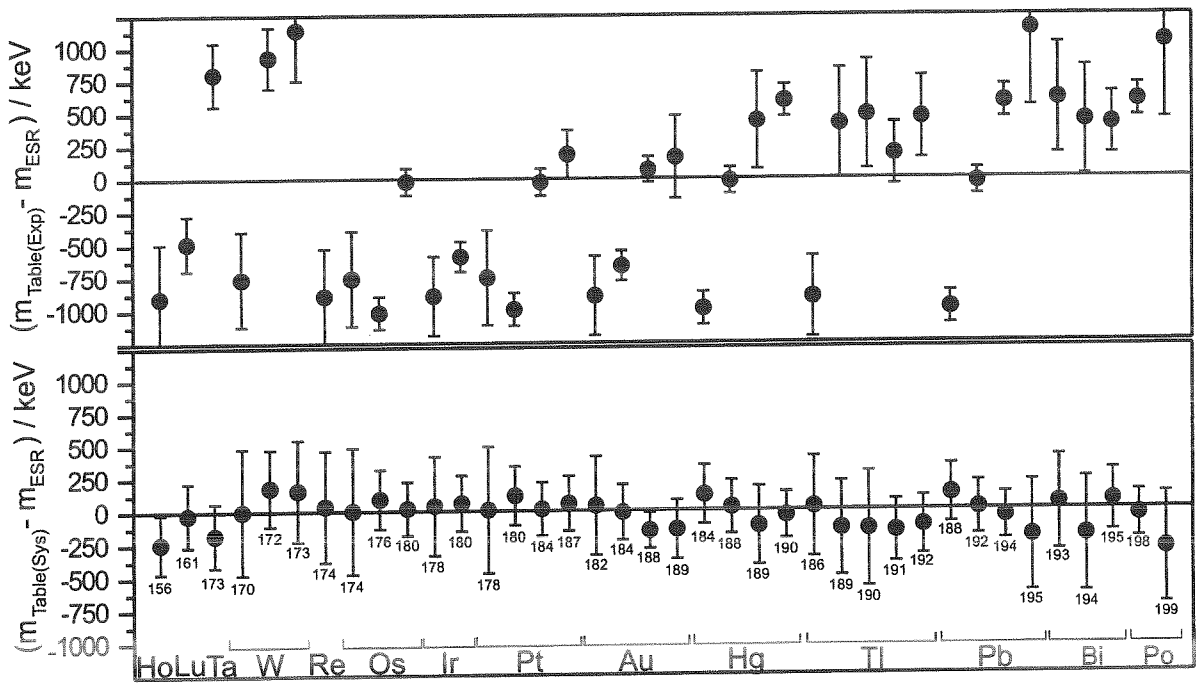

Figure 14: Comparison of previously measured mass data (top) [12] (p.479) and mass values recommended by Audi and Wapstra [12] (bottom) with our measured mass values.

The mass table of Audi and Wapstra is mainly a comprehensive compilation of experimental data which have been carefully evaluated [12]. From their least-square fit procedures the authors obtain by interpolation and extrapolation also predictions for the unknown masses. Therefore, it is interesting to compare our results with these predicted values. As a representative example we compare these predictions to our data for the nuclides of the elements W, Os and Pt . This demonstrates that predicted values of the table are in good agreement with our data.

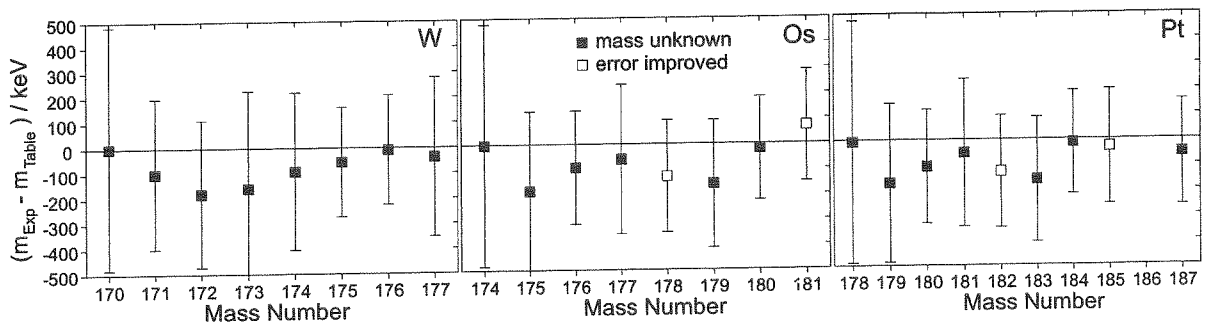

Figure 15: Differences of masses from our experiment obtained by Schottky spectrometry and from the Audi-Wapstra table [12] for the elements tungsten, osmium and platinum.

A check of the reliability of SMS mass data is a comparison (see Fig. 16) with mass

values obtained with the Penning trap mass spectrometer ISOLTRAP installed at ISOLDE/CERN [24],[25].

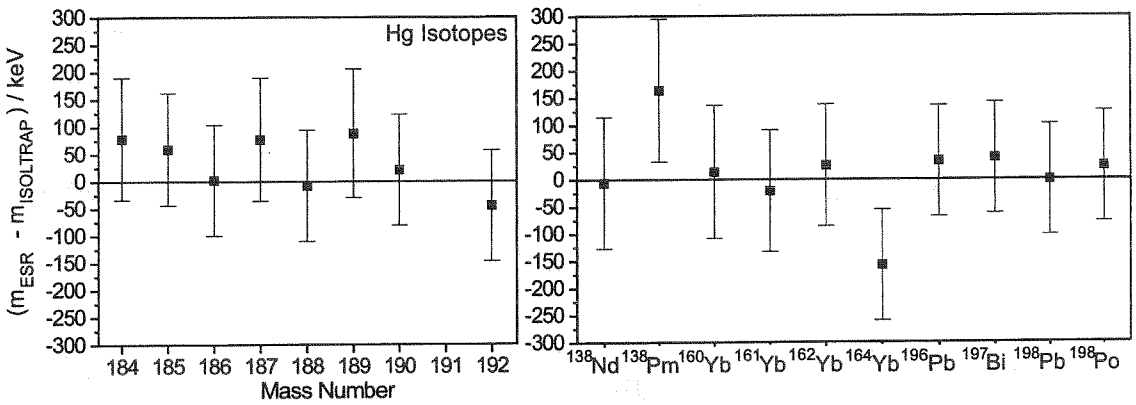

Figure 16: Differences of experimentally determined masses obtained by Schottky Mass Spectrometry and measurements performed by the Penning trap mass spectrometer ISOLTRAP for different isotopes of mercury (left panel) and isotopes of different elements [77] (right panel). In the case of ^{138}Pm most probably a mixture of the ground and the isomeric state was measured. The uncertainty of the ISOLTRAP values of 20–25 keV are included in the error bars.

In fig. 16 some of our data are compared to recent ISOLTRAP measurements [77]. The agreement of both experimental data sets is very good. An advantage of SMS is that a large mass surface can be mapped in one experiment whereas the ISOLTRAP can be tuned in an experimental cycle on a single isotope only. An ideal combination for mass research in unknown territories can be performed such that a few precisely measured reference masses are determined by a Penning trap system and with SMS a large mass surface is covered to study global structure effects (e.g. shell effects, shape changes etc.). A discussion of the features of both methods for mass measurements of exotic nuclei is given in reference [78].

A large number of mass models have been proposed and developed over the decades. They are based on different assumptions and can be categorized as follows:

- pure microscopic models, which start from the nucleon-nucleon interaction,
- macroscopic-microscopic models which use the modified liquid drop model with shell corrections,
- shell model predictions focused on narrow regions in the chart of the nuclides,,
- special mass relations combining masses of adjacent nuclides.

Critical assessments of nuclear mass models was done in refs. [79] -[82]). The most crucial test of the reliability of mass models are new experimental data in the regions of nuclides where masses have been unknown when the model was formulated.
Using the newly measured masses we can check the "extrapolability" of various mass formulae valid by the χ^2-criterion.

Table 10: Predictive power of various mass models. The rms-deviations in keV calculated for the set of: a) 1655 mass values of the 1986 Atomic Mass Table (taken from [80]), b) 175 masses measured from 1986 up to 1992 [80], c) experimental mass values of the 1995 Atomic Mass Table [12], d) 194 nuclides determined in this work, e) Theoretical deviation in keV obtained from the formula (37) for mass values of this work (see text).

Mass Formula	Type of the model	σ_{rms} (keV) a)	b)	c)	d)	χ^2	σ_{th} e)
Goriely [83]	Thomas-Fermi	-	-	732	646	42	640
Tondeur et al.[84]	Hartree-Fock	-	-	718	852	73	852
Duflo-Zucker[85]	microscopic approach	425	912	580	654	43	648
Möller-Nix[11]	macro- microscopic	827	1046	827	431	18	419
Möller et al.[11]	finite-range droplet and folded-Yukawa potential	766	1046	678	407	22	457
Spanier-Johansson [11]	liquid drop with correct.	697	1208	743	1195	147	1190
Satpathy-Nayak [11]	infinite nuclear matter	462	1529	691	1112	115	1108
Myers-Swiatecki [86]	Thomas-Fermi	-	-	698	417	18	406
Tachibana et al. [11]	empirical p-n interaction	506	834	547	718	52	711
Masson-Jänecke [11]	equation with isospin contributions	232	813	327	593	34	584
Jänecke-Masson [11]	mass relations	162	643	263	488	23	476
Comay-Kelson [11]	mass relations	269	795	350	532	28	521
Dussel et al.[11]	alpha-line systematics	288	288	318	198	3.8	169
Audi-Wapstra et al.[12]	extrapolations from experimental masses	-	-	-	138	1.9	95

To estimate the average deviation of the model σ_{th} we have used the expression

$$\frac{1}{n-1}\sum_{i=1}^{n}\frac{(M_{exp}-M_{th})_i^2}{(\sigma_{Mexp})_i^2+\sigma_{th}^2}=1. \qquad (37)$$

The value σ_{th} should be close to the usually used rms-deviation [11]

$$\sigma_{rms}^2=\frac{1}{n}\sum_{i=1}^{n}(M_{exp}-M_{th})_i^2, \qquad (38)$$

if σ_{Mexp}-values are less than the theoretical error. This is the case for all models.

The results of the "testing " of different model predictions [87] are presented in Table 10. Various types of theoretical approaches (both global and local) were chosen for comparison. In columns 3 ,4 and 5 the rms-data which were known before 1986, from 1986 to 1992 [80] and before 1995 ,respectively, are shown. The rms-values derived from

our new data alone are shown in column 6. These values were obtained on the basis of experimental values for 194 nuclides.
The χ^2 -values shown in the 7-th column of Table 10 have been determined from the formula (37) without the term σ_{th} in the denominator. The deviation of this factor from unity gives the scale of inaccuracy of the model. As one can seen from these values, only extrapolations of [13] satisfactorily predict our new experimental values.
The σ_{th} values are given in column 8. Since the experimental error bars are much less than theoretical one, the values for σ_{th} are close to the rms-deviations (compare columns 6 and 8).
Column 6 of Table 10 shows that none of the tested models (except of Dussel et al. local one) predict the new experimental data with an accuracy better than 400 keV. Comparing the rms-deviations for set of 1995 and new data, one finds that the majority of the models fits better to the previously known masses (to which they have been partly adjusted) than to the new data. This shows that the predictive power of these models is rather poor, at least in the region studied here. Only the models which use Thomas-Fermi calculations (Goriely et al. and Myers-Swiatecki) and the macro-microscopic approach (Möller-Nix and Möller et al.) show a better predictive power.
e

7 Physics insight into the proton-rich sub-uranium region

The large amount of new mass data shown in Table 4 allows a new look to some physics problems concerning nuclides far off the β -stability. These problems are discussed in the following subsections.

7.1 One-proton and two-proton drip-lines.

One of the exciting applications of the derived mass-surface is the possibility to identify the proton drip-line in the region of the chart of nuclides with $75 \leq Z \leq 91$.
Important work on this subject was done in investigations on proton radioactivity of some of the isotopes in the region $Z \leq 83$ [88]-[95].
We used the equation

$$S_p(Z,N) = B(Z,N) - B(Z-1,N) = (M(Z-1,N) + M(1,0) - M(Z,N))c^2 \quad (39)$$

to determine the pair of nuclides $(Z-1,N)$ and (Z,N) for which the proton separation energy S_p changes sign. Here B and M stand for the total binding energies and the atomic mass values of the nuclides, respectively.
We also derived the S_p-values for isomeric states. They have been determined from mass-values presented in Table 9.
Fig. 17 shows the values of separation energies obtained in this work for ground and isomeric states of isotopes of the elements from Tl to Pa.
As can be seen from this figure the position of the one-proton drip-line can definitely be identified for the region $83 \leq Z \leq 91$. For other Z-values we can give the interpolated (or extrapolated) results (see Fig. 18).
Thus, the proton drip-line has been identified for isomeric states as well. Note that

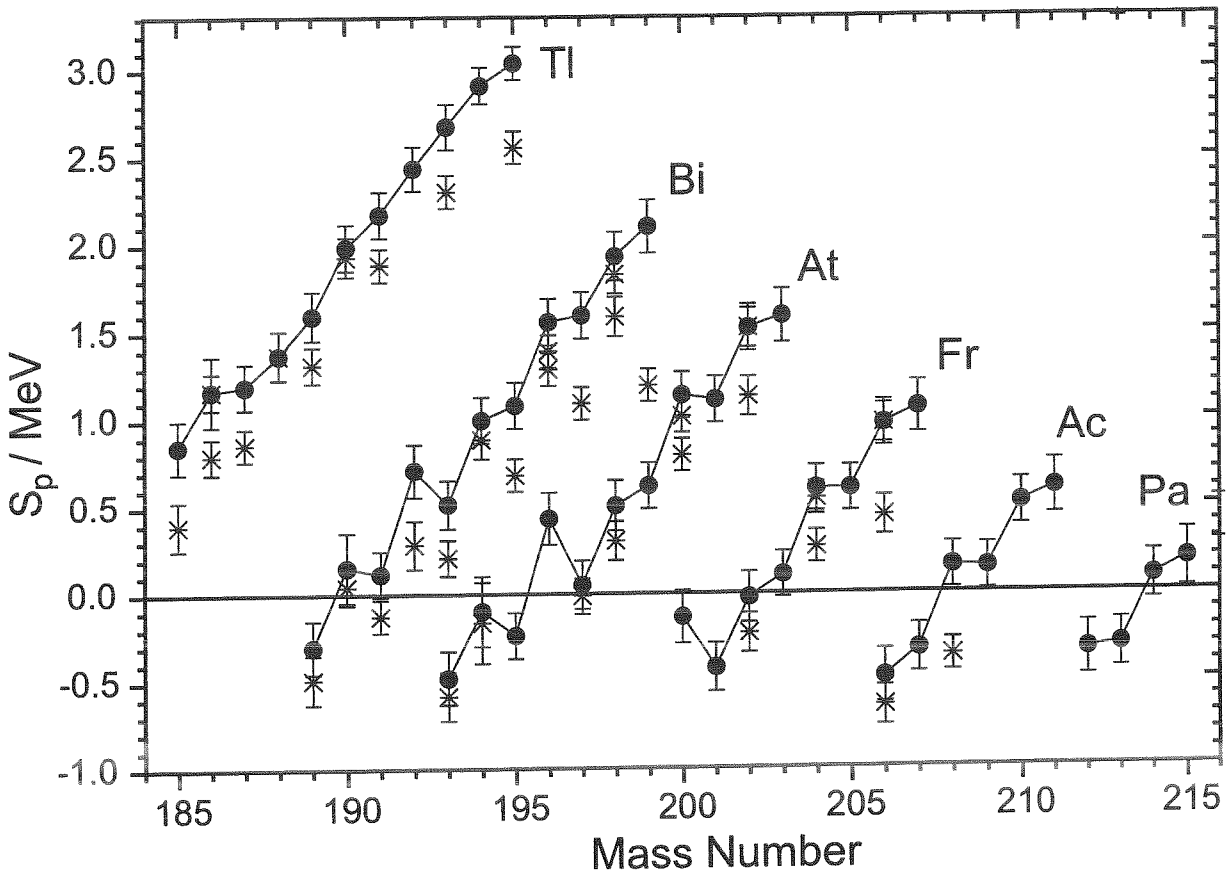

Figure 17: One-proton separation energies for odd-Z nuclides from Tl to Pa determined from the mass-values of this work. Ground states are marked by bold circles, whereas the isomeric states are indicated by asterisks

.

there are cases (^{191}Bi, ^{208}Ac and may be ^{202}Fr) where the isomeric states are proton-unbound, whereas the ground states are particle-bound (coexistence of a bound and an unbound long-lived proton state in one nuclide).

To determine the two-proton drip-line we used the expression

$$S_{2p} = B(Z,N) - B(Z-2,N) = (M(Z-2,N) + 2M(1,0) - M(Z,N))c^2. \qquad (40)$$

We have determined the values of the two-proton separation-energy S_{2p} for even-even nuclides and show them as a function of the mass number A in Fig. 19. One can use linear extrapolations of the behaviour of S_{2p} to zero to predict the two-proton drip-line. As can be seen from Fig. 19 the position of this line on the chart of nuclides can now be located in the region $74 \leq Z \leq 88$ and especially for mercury, lead and polonium isotopes.

Fig.20 summarizes the results in the chart of nuclides. The nuclides for which the mass values were determined for the first time are shown by grey squares. The positions of the one- and two-proton drip-line for ground states determined from experimental mass-data are shown. The known proton emitters are also indicated. We emphasize

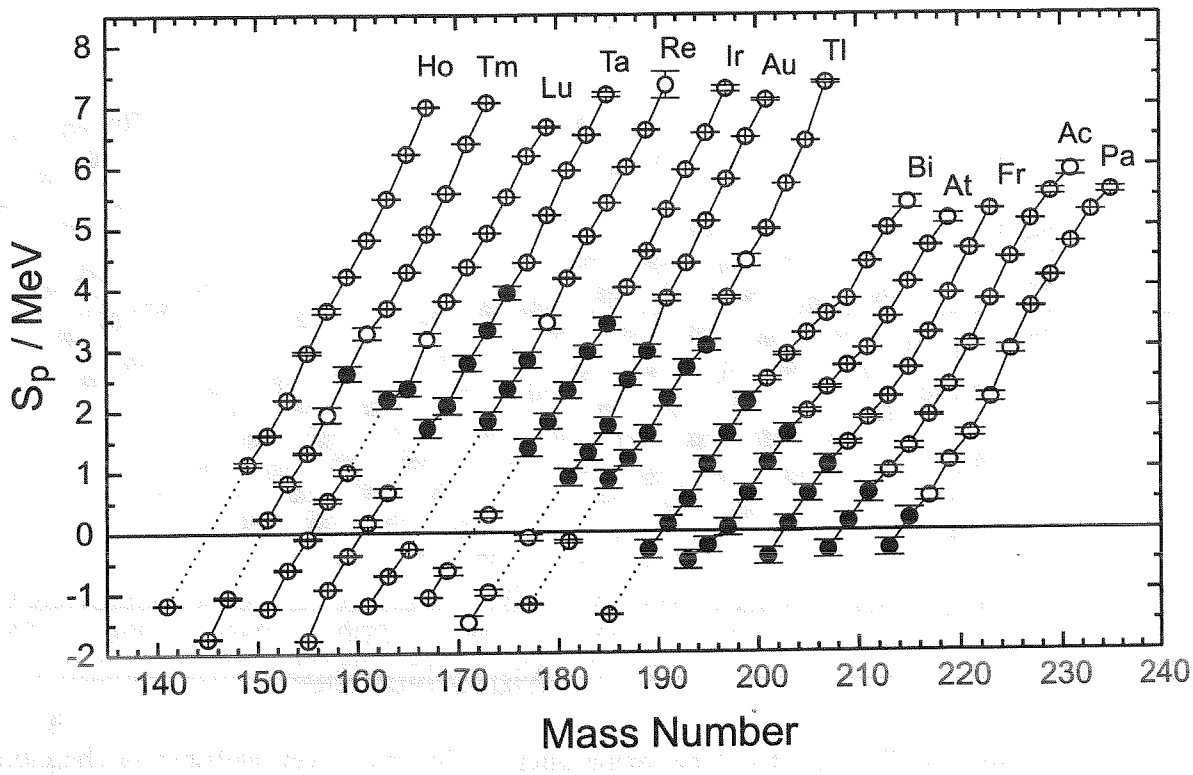

Figure 18: One-proton separation energies for odd-A and odd-Z isotopes of the elements from Ho to Pa determined in this work (full circles) and taken from [13] (open circles). The proton decay energies for ground states of proton unstable nuclides (open circles for negative S_p values) are taken from the refs.[88]-[95].

that the determination of the S_p-values and hence the border line is based only on the unambiguous data in Table 4. The S_{2p}- values were derived from the masses of even-even nuclides, which are definitely ground states.

The knowledge of the positions of the one- and two-proton drip-lines is important for the systematic search for proton radioactivity. The border of proton radioactivity can be roughly defined for nuclides with half-lives longer than 10^{-12} s, the approximate limit for the definition of radioactivity as such [98]. Then one can approximately determine the proton decay energy $Q_p = -S_p$, which corresponds to this half-life limit and, using the extrapolation of the S_p -data of Fig.18, the respective nuclei.

Spectroscopic information in this region of interest is extremely limited. Most of the nuclides have not been observed at all. Therefore, we used a simple approximation for the barrier penetration by protons which provides a satisfactory connection of Q_p and $T_{1/2}$ (see, e.g., [98]).

Without a centrifugal barrier for protons (l_p =0) we can write:

$$\lambda_p = \lambda_p^0 \cdot exp\Big\{-\frac{2(Z-1)e^2\sqrt{m_p}}{\hbar\sqrt{2B}} \cdot \Big(\sqrt{\frac{B}{Q_p}}arccos\sqrt{\frac{Q_p}{B}} - \sqrt{1-\frac{Q_p}{B}}\Big)\Big\}, \qquad (41)$$

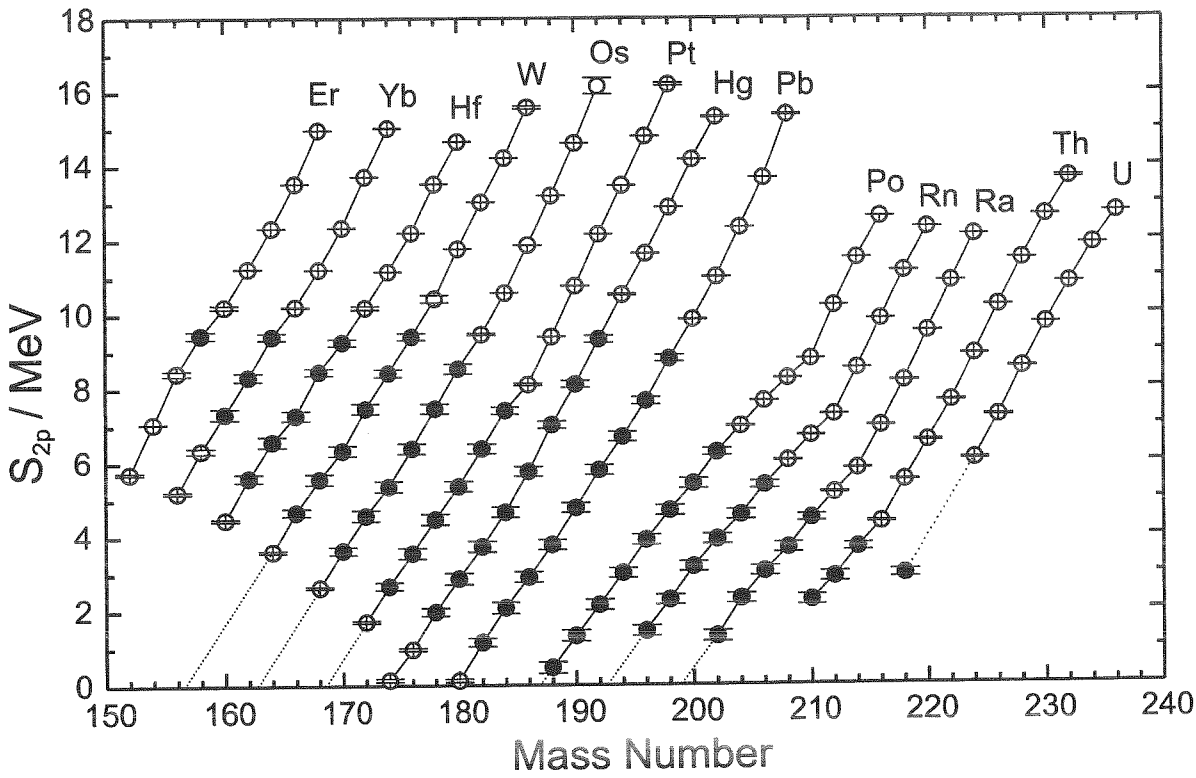

Figure 19: Two-proton separation energies for even-even isotopes of the elements from Er to U obtained in this work (full circles) and taken from ref.[13] (open circles). The dotted lines have been used for extrapolations or interpolations. The values for ^{174}Hg and ^{180}Pb have been determined by using the recent results of refs.[96, 97] and of ref.[13]

where λ_p^0 corresponds to nuclear lifetime 10^{-22} s and $B \simeq \frac{Z-1}{(1+(A-1)^{1/3})}$ stands for Coulomb barrier in MeV.

We used for our extrapolations a very rough dependence of S_p on A in the form $S_p = a + b \cdot A^{-1/3} + c \cdot A^{-1}$, which is based on the liquid-drop model. Extrapolated curves have been obtained by fitting only a restricted number of positive S_p-values closest to the proton drip-line. In this way, we avoid uncertainties from neglecting higher order terms in the formula used for S_p.
Fig.21 shows the size of the region of proton radioactivity, which might be called "littoral shallow" of the sea of instability (named "shallow waters" in [99]). The position of outer border of this "shallow" depends not only on Q_p-values, but also on the orbital angular momenta l_p of protons , which in our estimations were assumed to be zero. For isotopes of some of the elements (Ta, Re, Ir, Au and Tl) whose ground-states have spin value $1/2^+$ (see Fig.21) this is a reasonable assumption. For other elements the spin values of the nuclides are higher which can increase the half-lives and therefore will move the border away from the proton drip-line. The border shown in Fig.21 reflects the minimal size of the region of proton radioactivity.

For light and medium mass nuclides the "littoral shallow"should be smaller due to the

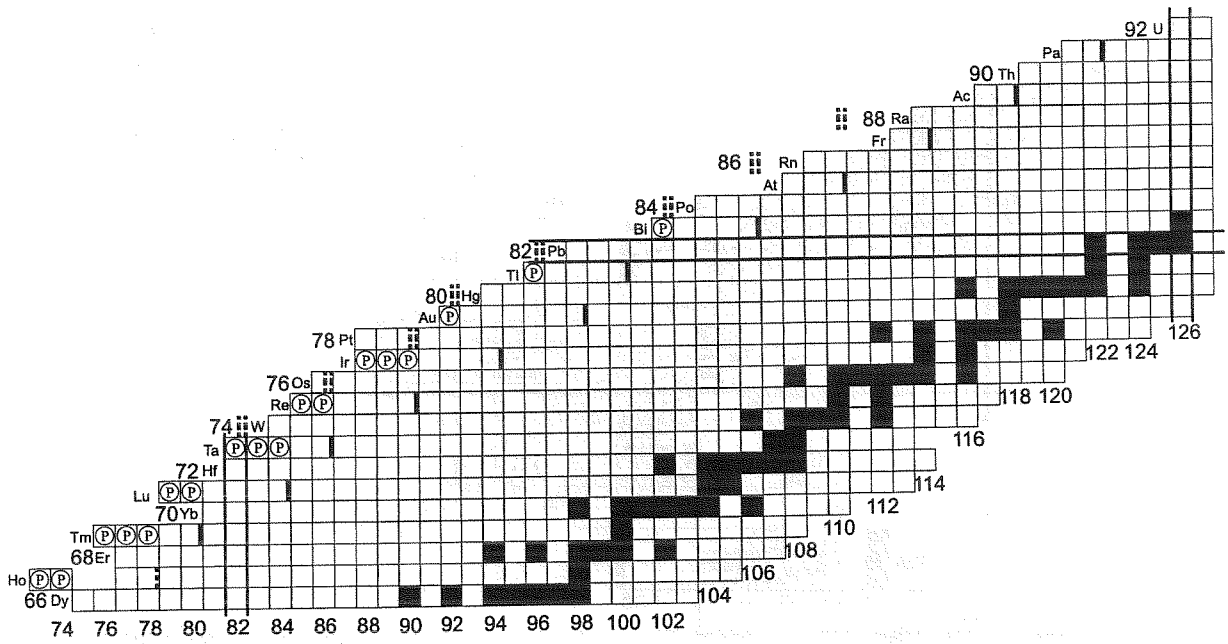

Figure 20: Part of the chart of nuclides. The nuclides whose masses were determined for the first time (or remeasured with better precision) are shown by grey squares. One- and two-proton drip-lines identified on the basis of experimental data obtained in this work are shown by single and by double vertical lines, respectively (dashed lines indicate the extrapolated or interpolated data). Known proton emitters are indicated by circles containing the letter "P".

lower Coulomb barrier which gives smaller Q_p-values for $T_{1/2} \simeq 10^{-12}s$.

7.2 On the problem of the Thomas-Ehrman shift in heavy nuclides

Our predictions of the position of the borders of the "littoral shallow" could be changed if a considerable shift of the proton separation energy would exist due to the so called Thomas-Ehrman (T.-E.) effect [100, 101]. The same changes due to the Coulomb correlations [102] should be expected for the proton drip-line. The knowledge of the position of the proton drip-line on the other hand is important for predictions of the path of rapid proton capture in stellar conditions. Since the position of the proton drip-line is still unknown for nuclides with Z $\geq$ 39 , there are uncertainties in the rp-path for sub-tin nuclides [103]. Thus, the existence (or nonexistence) of a T.-E. shift in medium and heavy nuclides is crucial. Since this effect was observed in very light mirror nuclides (^{13}C -^{13}N) as a relative shift of unbound analog states by $\simeq$ 700 keV, one might conclude that this phenomenon is a privilege of light nuclides (see also ref.[104]).
The T.-E. effect was explained as a reduction of Coulomb energy for proton-unbound states where the single particle wave function is pushed out of the nuclear interior. As the Coulomb barrier, which confines the wave function inside the nuclear interior, is small in light nuclides and the centrifugal barrier is usually small as well, it was thought

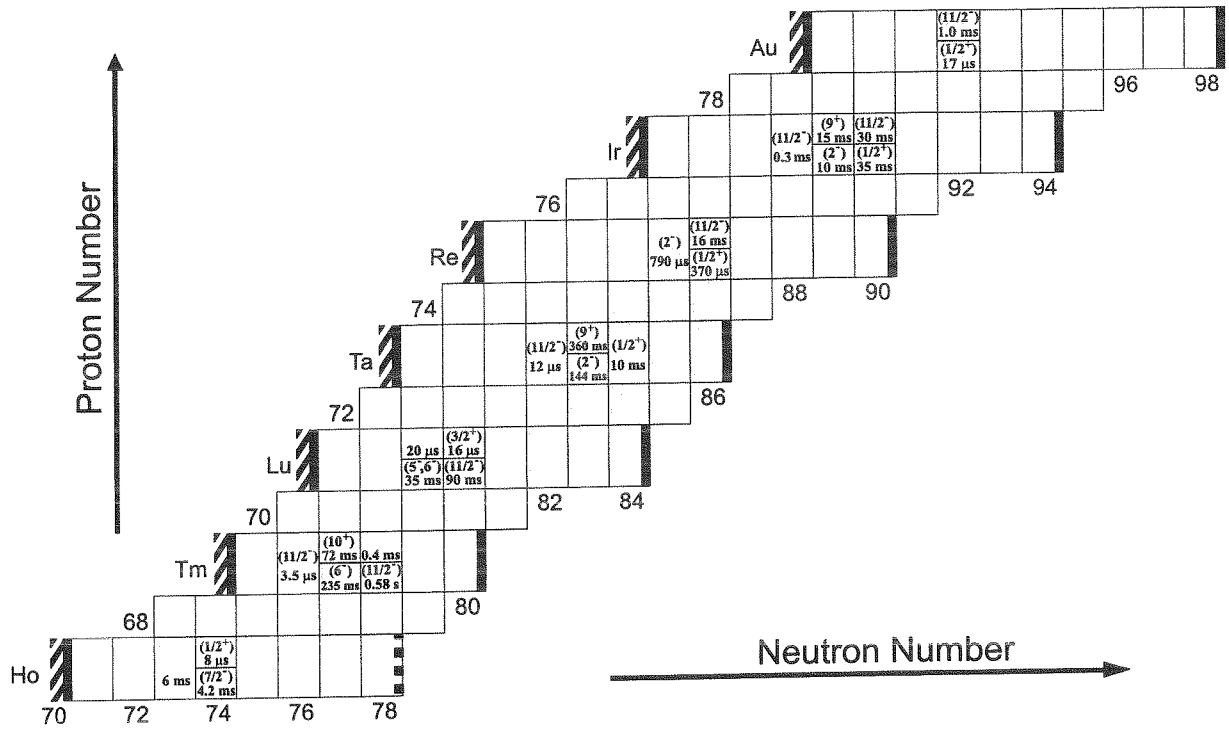

Figure 21: "Littoral shallow" on a part of the chart of nuclides. The proton drip-line is shown for odd-Z elements by vertical lines, whereas the outer border corresponding to $T_{1/2} = 10^{-12}$ s and $l_p = 0$ by bold lines with hetching. The known nuclides are given by grey squares. The spin and half-life values for known proton emitters are shown as well.

that the shift should be significant in light nuclear systems. This conclusion was supported by S-matrix calculations [105] which gave the estimation of the upper limit of the shift in terms of the width of the level.

The possibility to identify the T.-E. shift in the region of the proton drip-line in light and medium mass nuclides was formulated in [106]. The authors obtained on the average for proton-unbound nuclides a large difference of -576 keV between experimental and calculated mass values with a particular mass relationship [107]. On the other hand, the average difference for proton-bound nuclei was with 3.4 keV surprisingly small. Thus, an unambiguous manifestation of the T.-E. shift both in magnitude and in sign was claimed. A rather large difference of -234 ± 50 keV was determined for the medium-weight nuclide ^{39}Sc which has a small proton decay energy of about 450 keV and a high spin-value of $7/2^-$. Both characteristics would favor a small shift [108]. Recently [109, 110] a significant T.-E. shift was predicted for other medium-weight nuclides close to the proton drip-line.

The existence of the T.-E. shift could be seen in our data as a kink in the smooth behavior of the proton separation energies crossing the A-axis(S_p=0). If it exists, the bound proton ground states for odd-Z nuclides are shifted towards proton-rich side.

The new mass information obtained allows to perform this analysis. One needs to know S_p for proton-unbound nuclides and for a group of proton-bound isotopes close to the drip line. The odd-A proton-unbound isotopes of the elements Ta, Re, Ir, Bi^m and At

have the spin values equal to $1/2^+$. This strongly favors [108] a T.-E. shift because of the small angular momentum and the high value of the principal quantum number.

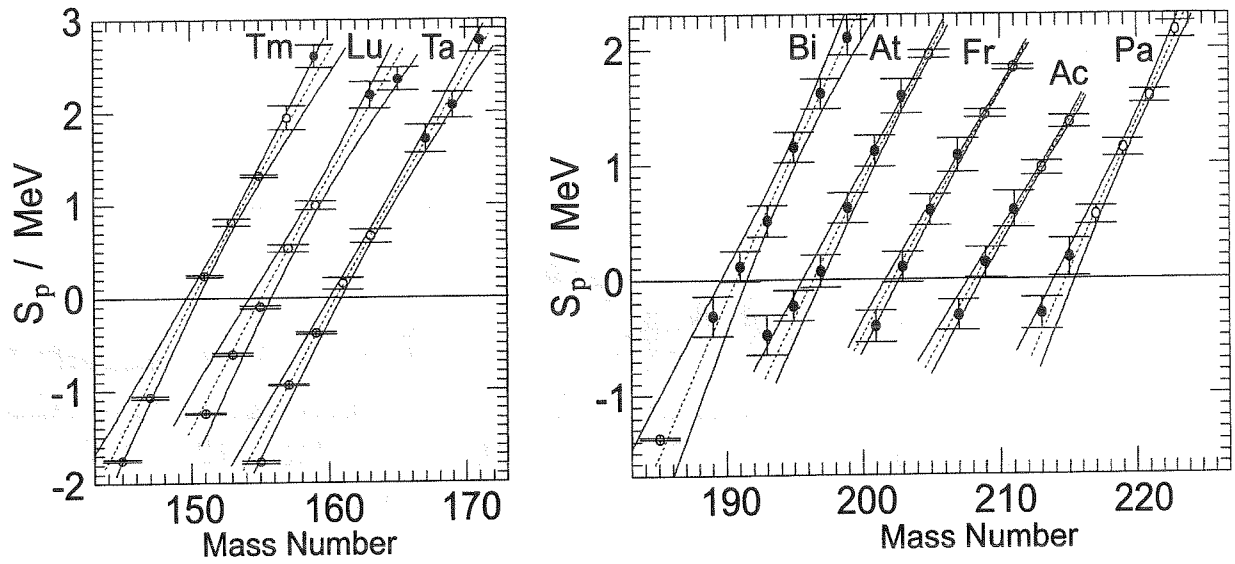

Figure 22: Fit of the proton separation-energies by polynomial function (dashed,see text). Only the points with positive S_p-values have been used for this procedure. The values determined in this work have been marked by full circles. The solid lines indicate the range of uncertainties.

The procedure of extrapolation has been described already in subsection 7.1 . The fitted curves are presented in Fig.22. This figure shows that the fit procedure is quite satisfactory for all presented cases. The average value for shifts of S_p from the extrapolated curves for all proton unbound nuclides turned out equal to (-20 ± 60) keV. Thus, we can conclude that there is no evidence for the existence of a Thomas-Ehrman shift in heavy nuclei.

7.3 Peculiar behavior of two-proton separation energies in the lead region

The experimental information about masses obtained in this work allows to determine the behavior of two-proton separation energies for nuclides far from the β-stability line. We can define

$$2G_p(Z,N) \equiv S_{2p}(Z,N) - S_{2p}(Z+2,N) = (M(Z-2,N) - 2M(Z,N) + M(Z+2,N))c^2. \quad (42)$$

For magic nuclides the quantity G_p defines the single particle shell gap. Changing the N-values for various Z-numbers (Z and N -even), we can see how the value G_p behaves moving away from N=126. The values of $2G_p$ derived from Table 4 are presented in Fig.23. One can see from this figure that the value of $2G_p$ reaches $\sim$ 7 MeV for the doubly magic nuclide ^{208}Pb due to the "mutual support" of two magic numbers [111]. However, it becomes much smaller in the region of N=106 ($2G_p \simeq 2.5$ MeV), which is

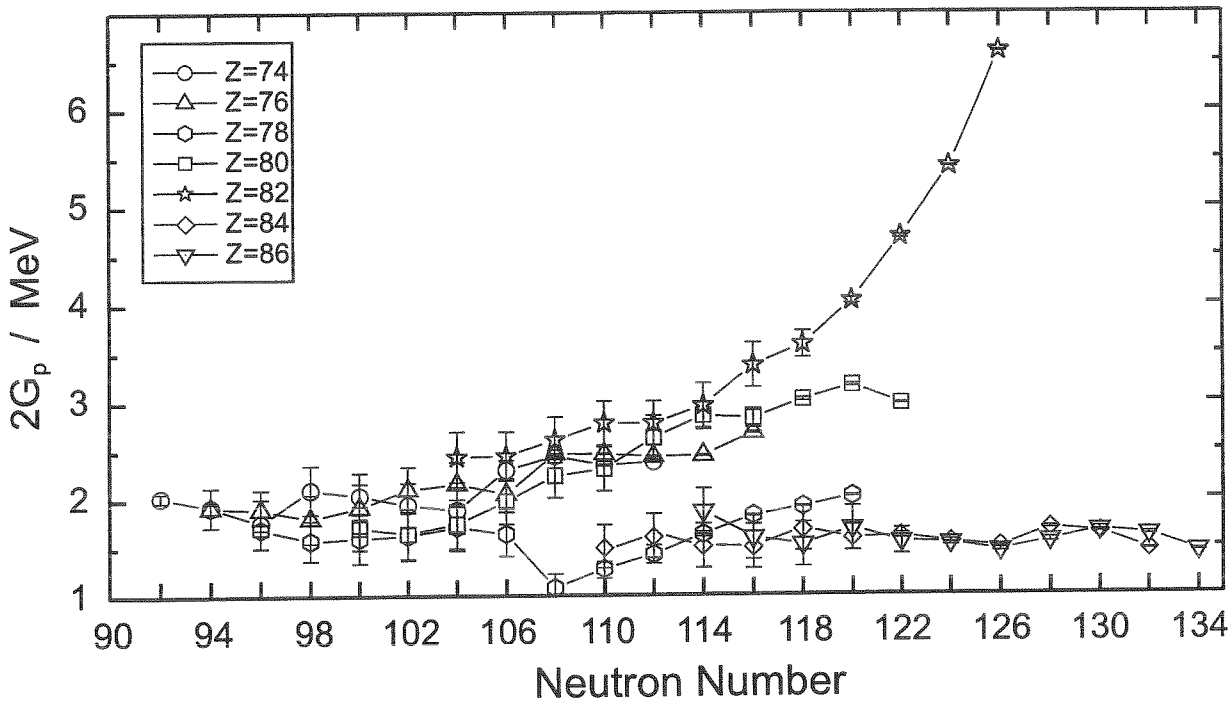

Figure 23: Differences between the two-proton separation energies $S_{2p}(Z,N) - S_{2p}(Z+2,N)$ for different Z-values in the vicinity of Z=82 as a function of N.

20 neutrons away from the magic number N=126.

A different trend can be observed for nuclides with other nucleon magic numbers. Fig.24 shows the behavior of the G_p gap for Z=50 nuclides close and far from stability and Figs.25 and 26 show the behavior of the G_n gaps around N=82 and N=126, correspondingly. The data for these figures have been taken from ref.[13].
The G-values for Z=50 and N=82 nuclides remain big also far from the β-stability line, whereas there is not enough information available for N=126 nuclides . At least, within the known mass region there is no indication yet for a strong quenching of the G_n for N=126 nuclides. Thus, the G_p quenching phenomenon illustrated above for Z=82 nuclides is a peculiar feature of this Z-value.

The observed phenomenon of G_p quenching contributes to the discussion about universality of the magic numbers (see,e.g.,[112]). We cannot exclude that some proton and neutron magic numbers can disappear and others can appear very far from the region of β -stability. Such a possibility has been investigated on a theoretical basis (see, e.g. [113, 114, 115] and references herein). The most dramatic disagreement of various predictions concerns the magic proton number Z=82, where contradictory predictions have been presented concerning the shell-closure effect ([113] and [114]). Similar disagreement in the conclusions concerning a possible quenching of magicity of Z=82 far off the β-stability line exists in the interpretation of various experimental results of α-decay ([116, 117, 118] and references herein).
Possible reasons for the strong decrease of G_p towards the proton drip-line could be changes in the shape of nuclides, changes in correlation energies or a lowering of the

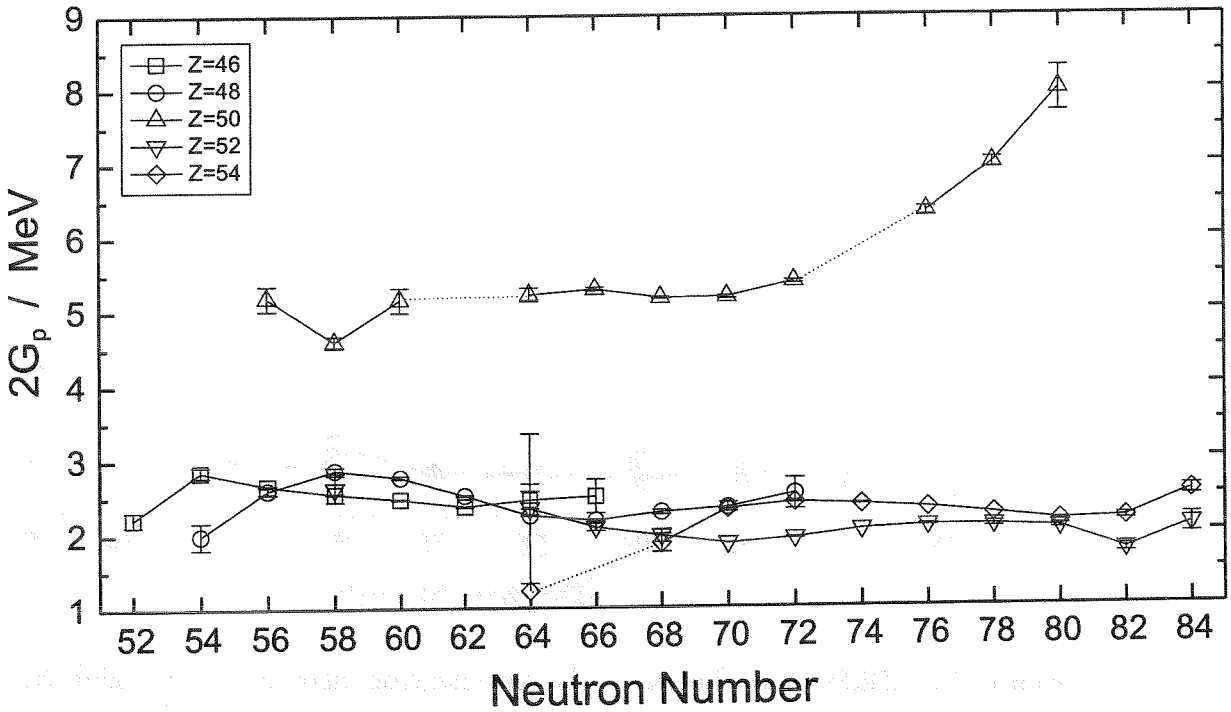

Figure 24: Differences between the two-proton separation energies for different Z-values in the vicinity of Z=50 as a function of N.

energies of single particle intruder states [113].
The last reason could be due to relative shifts of the single-particle levels because of a "synchronous" occupation of high(low) spin levels by neutrons and protons [113]. For example, the high–spin neutron filling for N$\leq$ 114 can cause a drop of the high-spin proton levels.

8 Conclusion and Outlook

The combination of the fragment separator FRS and the storage cooler ring ESR is a unique and universal tool to study nuclear properties of relativistic projectile fragments. First comprehensive results on precise mass measurements of exotic nuclei stored and cooled in the ESR at 330–370 MeV/u are presented in this paper. A large number of different isotopes in a cocktail beam of fragments can be simultaneously stored and cooled in the ESR. The calibration with many reference masses in the same spectrum is advantageous with respect to the minimization of systematic errors. SMS has a high sensitivity and in the limit the revolution frequency of a single ion can be observed. In the present experiment, the masses of nuclides with half-lives as short as 10 s could be determined which is mainly limited by the electron cooling time.
An advantage of SMS is that a large mass surface can be mapped in one experiment whereas, e.g., the ISOLTRAP can be tuned in an experimental cycle on a single isotope only. An ideal combination for mass research in unknown territory can be performed such that a few precisely measured reference masses are determined by a Penning trap

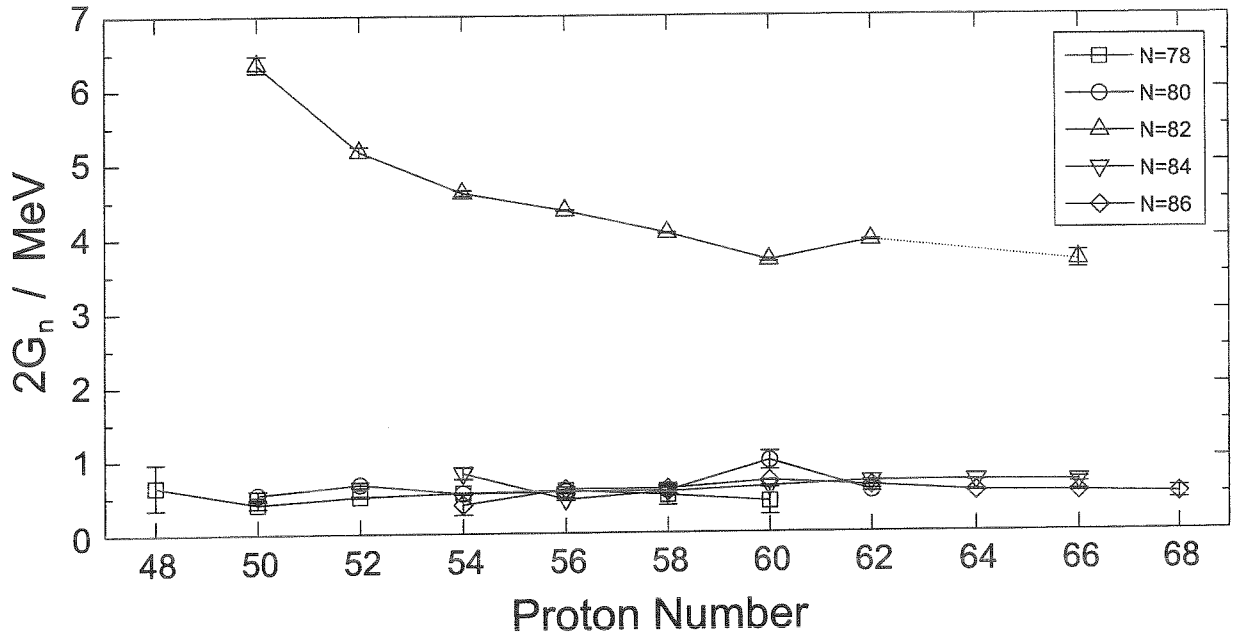

Figure 25: Differences between the two-neutron separation energies $S_{2n}(Z,N) - S_{2n}(Z,N+2)$ for different N-values in the vicinity of N=82 as a function of Z.

system and with SMS a large mass surface is covered to study global structure effects e.g., shell effects and shape changes. A discussion of the features of both methods for mass measurements of exotic nuclei is given in reference [78].

The new mass data obtained by SMS at GSI have opened a considerable extension of mass mapping into an exotic territory of the chart of nuclides. This extension has been done by means of network of α-decay energies that allowed to connect the region of measured nuclides with exotic nuclides very far of β-stability.

In total, mass values for 168 neutron-deficient nuclides in the region $57 \leq Z \leq 92$ have been determined for the first time. They are marked in Fig. 27 with a grey squares.

The masses for 60 isomeric states of exotic nuclides with so far unknown excitation energies, have also been determined.

The new numerous data on the masses of exotic short-lived nuclides led to a new insight into the physics of exotic nuclides.

A part of the mapped surface belongs to the area of proton-instability. The proton drip-line has been determined by our experimental data. A position of the two-proton drip-line has been obtained by extrapolations. The region of proton-radioactive nuclei between holmium and gold has been outlined. The border of this so called "littoral shallow of the sea of instability" is 6 to 10 neutron numbers away from the proton drip-line for odd-Z nuclides. A considerable part of the nuclides belonging to the short-lived proton-emitters, is still unknown. The knowledge of the size of this particular region of the chart of nuclides is useful in planning and understanding of experiments on proton radioactivity.

The analysis of the experimental data shows that there is no Thomas-Ehrman shift in a wide region of heavy nuclides, which could change the position of the proton drip-line.

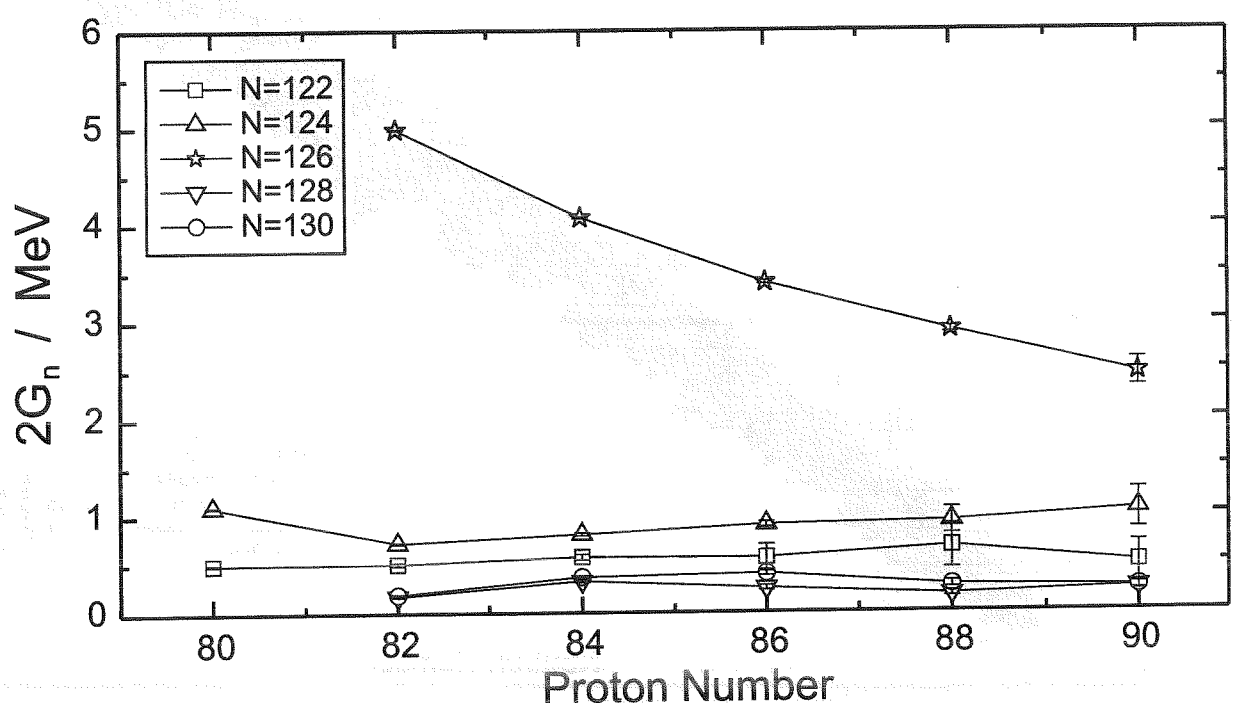

Figure 26: Differences between the two-neutron separation energies for different N-values in the vicinity of N=126 as a function of Z.

One of the exciting problems discussed over the years is the "universality" of the well known magic proton and neutron numbers throughout the chart of nuclides. We observed a washing out of the two-proton separation energy gap for lead nuclides far off the β-stability line.
The predictive power of different theoretical mass formulae is of importance for Nuclear Physics and Astrophysics. We has been checked it on the new mass-surface for 13 different mass models. The result of this comparison shows that neither of the mass formula tested (except of Dussel et al.local one) yields mass values with an accuracy better than $\sim$ 0.4 MeV. The extrapolations of Audi-Wapstra [12] satisfactorily agree with our experimental values.

The combination of direct mass measurements and α-decay spectroscopy used in this work allowed to map a wide range of α-emitters. This approach will be extended in our future experiments.

Since the first SMS-measurements have been performed as described in this article a number of important improvements for SMS could be achieved [119, 120]. The performance of the ESR cooler was considerably improved yielding a stronger cooling force which led to shorter cooling times and, therefore, gave access to isotopes with slightly shorter half-lives. Furthermore, the better stabilization of the power supplies and the improved field homogeneity of the ESR magnets helped to improve the resolving power by more than a factor 2 in the mass spectra [46]. A new data acquisition system was taken into operation where the digitized signals of the Schottky probes were recorded

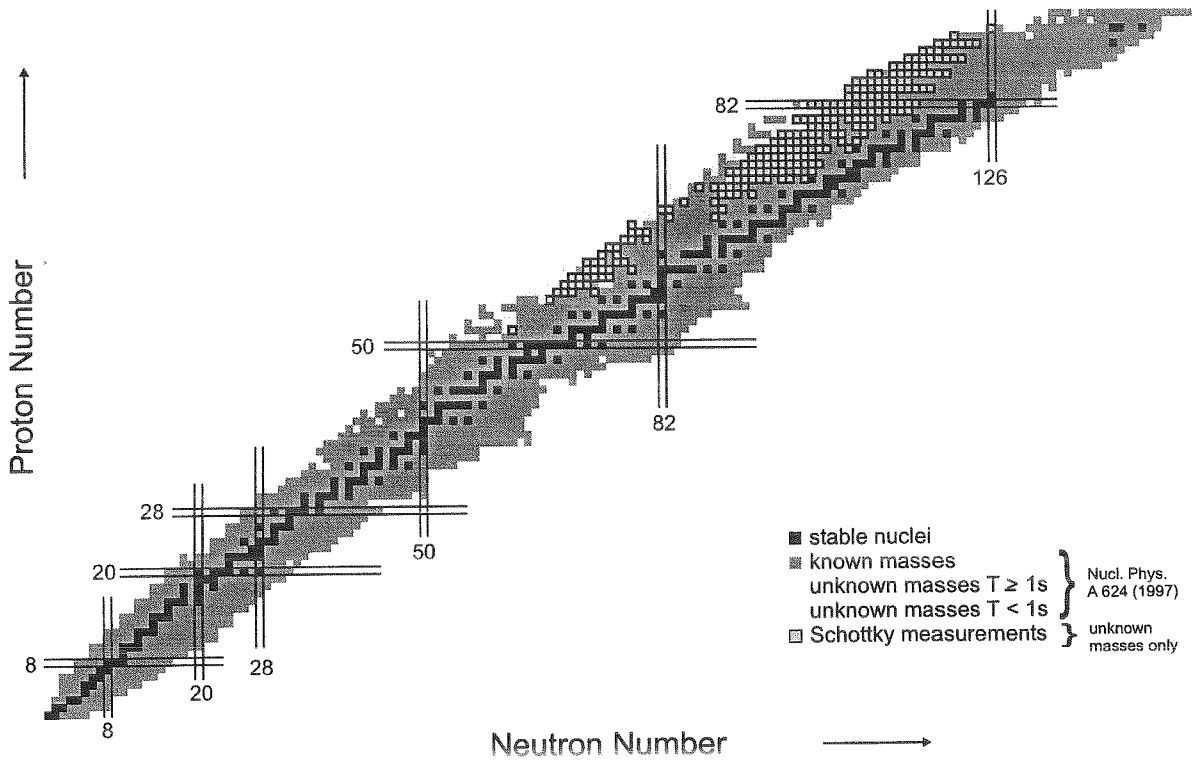

Figure 27: Chart of nuclides with known and unknown masses illustrated according to [13]. The nuclides with previously unknown masses that have been determined in this work are marked with a grey squares.

sequentially [120]. The fast Fourier transformation of these time-correlated data can be performed off-line which gives the advantage that possible drifts during the measurement can be corrected. The new set of data is presently under analysis. Exotic nuclei with half-lives shorter than the cooling time can be investigated by the time-of-flight techniques where the ESR is operated in the isochronous mode [121, 122, 123]. In this case, the magnetic fields of the ESR quadrupole and hexapole magnets are set such that the revolution frequency of an ion species becomes independent of its velocity spread, see equation (2). This novel experimental technique has been successfully applied in first measurements with nickel [124, 46], chromium and kripton fragments ($T_{1/2} < 100$ ms) [125].

In the future, direct mass measurements will be extended to shorter-lived nuclei using the isochronous method. However, there are also regions on the chart of nuclei where the Schottky mass spectrometry can significantly contribute to improve the knowledge of the mass surface. The better mass resolution as well as the successful development of stochastic cooling in the ESR [126], and the use of high-sensitive resonant Schottky-probes will considerably enhance the potential of Schottky mass spectrometry of exotic nuclei.

Acknowledgements

The authors would like to thank G. Audi, M. Bender, T. Enqvist, H. Kettunen, M. Leino, J.A. Maruhn, P. Ring, H. Schatz, K.-H. Schmidt, V. Shaginyan, A. Sobiczewski,

J. Stadlmann and W. Swiatecki for fruitful discussions. This work has been financially supported by BMBF under Contract No. 06 GI 4751 and No. 06 LM 363, and the Beschleunigerlaboratorium München. Yu. L. and Yu. N. would like to thank GSI and the II. Physics Institute of the Giessen University for warm hospitality as well as the WTZ fund for financial support under grant No. RUS-654-96. Z.P. would like to acknowledge the GSI for warm hospitality and Polish Committee for Scientific Research (KBN) for support under grant No. 2P03B 117 15.

References

[1] G. Audi and A.H. Wapstra, Nucl. Phys. **A 565**, 1 (1993).

[2] W.J. Swiatecki, Nucl. Phys. **A 574**, 233c (1994).

[3] P. Franzini and L.A. Radicati, Phys. Rev. Lett.**6**, 322 (1963).

[4] Yu.V. Gaponov *et al.*, Nucl. Phys. **A 391**, 93 (1982).

[5] W. Myers and W. Swiatecki, Ann. Phys. **55**, 395 (1969)

[6] W. Myers and W. Swiatecki, Nucl. Phys. **A 612**, 249 (1997).

[7] A. Bulgac and V. Shaginyan, Nucl. Phys. **A 601**, 103 (1996).

[8] M. Bender, Doctoral Thesis, Frankfurt University (1998).

[9] W.D. Myers, W.J. Swiatecki, Phys. Rev. **C 58**, 3368, (1998).

[10] P. Ring, contribution to ENAM-98 Conf.(1998).

[11] P.E. Haustein, ed. Atom. Data Nucl. Data Tables, **39**, 185 (1988)

[12] G. Audi and A.H. Wapstra, Nucl. Phys. **A 595**, 409 (1995).

[13] G. Audi *et al.*, Nucl. Phys. **A 624**, 1 (1997).

[14] W. Mittig *et al.*, Ann. Rev. Nucl. Sci. **47**, 27 (1997).

[15] R. Klapisch *et al.*, Phys. Rev. Lett.,**31**, 118 (1973).

[16] W. Mittig. Nucl. Phys. **A 553**, 473c (1993).

[17] I. Bergström *et al.*, Physica Scripta **T 59** 1995

[18] H.J. Kluge, Proc.ENAM-95 Conf.,Editions Frontiers, 3, (1995)

[19] J.M. Wouters *et al.*, Nucl. Instr. Meth. **B 26**, 286 (1987)

[20] A. Gillibert *et al.*, Phys. Lett. **B 176**, 317 (1986).

[21] G. Auger *et al.*, Nucl. Instr. Meth. **A 350**, 235 (1994).

[22] A. Lepine-Szyly *et al.*, Proc.ENAM-95 Conf., 79 (1995).

[23] S. Issmer *et al.*, Eur. Phys. J. **A 2**, 173 (1998).

[24] G. Bollen *et al.*, Nucl. Instr. Meth. **A 368**, 675 (1996).

[25] D. Beck *et al.*, Eur. Phys. J. **A 8**, 307 (2000).

[26] B. Franzke, H. Geissel and G. Münzenberg. Mass measurements of stored fragments, GSI-proposal (1987).

[27] K. Blasche *et al.*. Proc.of the 3-rd European Part.Acc.Conf., Berlin (1992) p.9, and M. Steiner *et al.*. Nucl. Instr. Meth. **A 312**, 420 (1992).

[28] H. Geissel *et al.*, Nucl. Instr. Meth. **B 70**, 286 (1992).

[29] B. Franzke, Nucl. Instr. Meth. **B 24**, 18 (1987).

[30] M. Steck *et al.*, Phys. Rev. Lett. **77**, 3803 (1996).

[31] B. Franzke, Nucl. Instr. Meth. **B 24**, 18 (1987).

[32] H. Geissel, *et al.*, Phys. Rev. Lett. **68**, 3412 (1992).

[33] H. Irnich *et al.*, Phys. Rev. Lett. **75**, 4182 (1995).

[34] Th. Beha. Doctoral Thesis, University of München, 1995.

[35] T. Radon *et al.*. Nucl. Phys. **A 677**, 75 (2000).

[36] Th. Kersher. Doctoral Thesis. University of München, 1996.

[37] T. Radon. Doctoral Thesis. University of Giessen, 1998.

[38] Yu.N. Novikov *at al.*. Nucl. Phys. **A** (to be published)

[39] C. Scheidenberger *et al.*, Nucl. Instr.Meth. **B 142**, 441 (1998) .

[40] K. Sümmerer *et al.*, Phys. Rev. **C42**, 2546 (1990).

[41] N. Iwasa *et al.*, Nucl. Instr. Meth. **B 126**, 284 (1997).

[42] J. Borer *et al.*, *Proc. IXth Conf. on High Energy Accelerators*, Stanford 1974, p.53 (1974).

[43] T. Radon *et al.* Phys. Rev. Lett. **78**, 4701 (1997)

[44] B. Franzke, Physica Scripta **T 59**, 176 (1995).

[45] B. Schlitt *et al.*, Hyp. Int. **99**, 117 (1996) and Nucl. Phys. **A 626**, 315c (1997)

[46] H. Geissel *et al.*, ENAM-98 AIP Conf.Proceedings, 455, 11 (1998).

[47] K.N. Huang *et al.*, At. Data Nucl. Data Tables **18**, 243 (1976)

[48] W.R. Johnson and G. Soff. At. Data Nucl. Data Tables **39**, 265 (1988)

[49] D.R. Plante *et al.*, Phys. Rev. **A 49**, 3519 (1994).

[50] J.E. Freund,*Mathematical Statistics*, ed. by Prentice-Hall, Inc., Englewood Cliffs, N.J. (1971).

[51] G. Bollen *et al.*, Phys. Rev. **C 46**, R2140 (1992).

[52] *Numerical Recipies.* Cambridge University Press, 1992.

[53] G. Audi and A.H. Wapstra. Proc.ENAM -95 Conf., Edition Frontiers, p.13 (1995).

[54] A. Rytz, Atom. Data Nucl. Data Tables **47**, 205 (1991).

[55] Nuclear Data Sheets (1986-2000).

[56] Y.A. Akovali, Nucl. Data Sheets **84**, 1 (1998).

[57] J.C. Batchelder *et al.*, Phys. Rev. **C 54**, 949 and 2041 (1996).

[58] T. Enqvist, Doctoral Thesis, Jyväskylä University report N3, 1996.

[59] T. Enqvist *et al.*, Z. Phys. **A 354**, 1 (1996).

[60] T. Enqvist *et al.*, Z. Phys. **A 354**, 9 (1996).

[61] H. Ikezoe *et al.*, Phys.Rev. **C 54**, 2043 (1996).

[62] M. Leino *et al.*, Z. Phys. **A 355**, 157 (1996).

[63] R.B.E. Taylor *et al.*, Phys. Rev. **C 54**, 2926 (1996).

[64] J.C. Batchelder *et al.*, Z. Phys. **A 357**, 121 (1997) and Phys. Rev. **C 55** R2142 (1997).

[65] S. Mitsuoka *et al.*, Phys. Rev. **C 55**, 1555 (1997).

[66] Y.H. Pu *et al.*, Z. Phys. **A 357**, 1 (1997).

[67] J. Wauters *et al.*, Phys. Rev. **C 55**, 1192 (1997).

[68] A.N. Andreyev *et al.*, Z. Phys. **A 358**, 63 (1997).

[69] K. Eskola *et al.*, Phys. Rev. **C 57**, 417 (1998).

[70] A.N. Andreyev *et al.*, Phys. Rev. Lett. **82**, 1819 (1999) and Acta Phys. Polonica **30**, 1255 (1999).

[71] A.N. Andreyev *et al.*, Eur. Phys. J.**A 6**, 381 (1999).

[72] M.B. Smith *et al.*, Eur. Phys. J. **A 5**, 43 (1999) and J. Phys. **G 26**, 787 (2000).

[73] A.N. Andreyev *et al.*, Nature **405**, 430 (2000).

[74] H. Kettunen *et al.*,(to be published in 2001).

[75] G. Audi *et al.*, Nucl. Instr. Meth. **A 249**, 443 (1986).

[76] M. de Jong *et al.*, Nucl. Phys. **A 613**, 435 (1997).

[77] S. Schwarz, Doctoral Thesis, University of Mainz, 1998.

[78] H. Geissel *et al.*, Nucl. Instr. and Meth. **B 126**, 351 (1997).

[79] P.E. Haustein, Proc. AMCO-7 Conf., Darmstadt, p.413 (1984).

[80] C. Borcea and G. Audi, CSNSM-report 92.38 (1992).

[81] P.Möller and J.R. Nix, Inst.of Phys.Conf.,series No.132, p.43 (1993).

[82] Z. Patyk *et al.*, GSI-preprint 97-40 (1997).

[83] S. Goriely, http://www-astro.ulb.ac.be.

[84] F.Tondeur *et al.* Phys. Rev., **C 62**, 024308 (2000) and http://www-astro.ulb.ac.be.

[85] J. Duflo and A.P. Zuker. Phys. Rev. **C 52**, R23 (1995).

[86] W.D. Myers and W.J. Swiatecki. LBL - 36803, 1994.

[87] *The Isotopes Project Home Page/Atomic masses,* http://ie.lbl.gov/toimass.html.

[88] J. Batchelder *et al.*, Phys. Rev. **C 57**, R1042 (1998).

[89] R. Irvine *et al.*, Phys. Rev. **C 55**, R1621 (1997).

[90] C.Davids *et al.*, Phys. Rev. Lett. **76**, 592 (1996).

[91] C. Davids *et al.*, Phys. Rev. **C 55**, 2255 (1997).

[92] C. Davids *et al.*, Phys. Rev. Lett. **80**, 1849 (1998).

[93] J. Uusitalo *et al.*, Phys. Rev. **C 59**, R2979 (1999).

[94] G. Poli *et al.*, Phys. Rev. **C 59**, R2975 (1999).

[95] K. Rykaczewski *et al.*, Phys. Rev. **C 60**, 011301-1 (1999).

[96] J. Uusitalo *et al.*, Z. Phys. **A 358**, 375 (1997).

[97] C.R. Bingham *et al.*, Proc.AIP-Conf.(Feb.97), **392(1)**, 341 (1997).

[98] V.I. Goldanskii, Ann. Rev. Nucl. Sci. **16**, 1 (1960).

[99] W. Greiner, Int. J. Mod. Phys. **5**, 1 (1995).

[100] J.B. Ehrman, Phys. Rev. **81**, 412 (1951).

[101] R.G. Thomas, Phys. Rev. **88**, 1109 (1952).

[102] A. Bulgac and V.R. Shaginyan. Eur. Phys. J. **A 5**, 247 (1999) and Phys. Lett. **B 269**, 1 (1999).

[103] H. Schatz *et al.*, Phys. Rev. **C 294**, 167 (1998).